



High-resolution 3D numerical modeling of thrust wedges: Influence of décollement strength on transfer zones

Jonas B. Ruh, Taras Gerya, and Jean-Pierre Burg

Department of Earth Sciences, ETH Zurich, Zurich, Switzerland (jonas.rub@erdw.ethz.ch)

[1] The mechanics and dynamics of thin-skinned compressible thrust wedges with prescribed offsets in the backstop, i.e., transfer zones, are investigated using a three-dimensional finite difference numerical model with a visco-brittle/plastic rheology. The main questions addressed are as follows: (i) What is the influence of the initial length of the backstop offset and (ii) what is the effect of the frictional strength of the main décollement on the structural evolution of the brittle wedges along such transfer zones? Results show that the shorter the backstop offset, the earlier these two thrust planes connect, forming a curved frontal thrust along the entire width of the model. Younger, in-sequence thrusts are formed parallel to this curved shape. Long backstop offsets produce strongly curved thrust faults around the indenting corner. Simulations with a weak basal friction evolve toward almost linear frontal thrusts orthogonal to the bulk shortening direction. Increased basal drag in models with a strong décollement favors propagation of the backstop offset into a transfer zone up to the frontal thrust. These simulations revealed that surface tapers of the wedge in front of the backstop promontory are larger than what the critical wedge theory predicts, whereas the tapers on the other side of the transfer zone are smaller than analytical values. This difference is amplified with increasing length of the backstop offset and/or strength of the décollement. Modeled surface elevation schemes reproduce well the topographic patterns of natural orogenic systems such as the topographic low along the Minab-Zendan transform/transfer fault between the Zagros and Makran.

Components: 12,000 words, 19 figures, 2 tables.

Keywords: transfer zones; thin-skinned; thrust wedge; numerical modeling; accretionary wedge.

Index Terms: 4255 Oceanography: General: Numerical Modeling (0545, 0560, 1952); 8004 Structural Geology: Dynamics and mechanics of faulting (8118) (8118); 8108 Tectonophysics: Continental tectonics: compressional; 8115 Tectonophysics: Core processes (1213, 1507).

Received 21 November 2012; **Revised** 4 February 2013; **Accepted** 4 February 2013; **Published** 29 April 2013.

Ruh, J. B., T. Gerya, and J.-P. Burg (2013), High-resolution 3D numerical modeling of thrust wedges: Influence of décollement strength on transfer zones, *Geochem. Geophys. Geosyst.*, 14, 1131–1155, doi:10.1002/ggge.20085.

1. Introduction

[2] Plastic thrust wedges such as submarine accretionary wedge systems or compressional thin-skinned fold-and-thrust belts have been intensely studied over several decades, in particular since the application of the critical taper theory [e.g., Dahlen, 1990; Platt,

1990; Stockmal, 1983; Westbrook and Smith, 1983]. Accretionary wedges and fold-and-thrust belts are related to convergence subduction and/or continental collision tectonics and develop by scraping an upper crustal rock sequence off the subducting oceanic or converging continental plate along a weaker basal décollement. Such major décollements are often

water saturated, overpressured shale layers that can be treated as frictional material [Kopf and Brown, 2003; Saffer et al., 2001; Takahashi et al., 2007; Wang et al., 1980]. Shortening of the compressed sedimentary sequence develops in-sequence thrusting, ultimately forming an imbricate fan. Isolated out-of-sequence thrusts may appear at the rear of the wedge [Morley, 1988; Storti and McClay, 1995]. Folds and thrusts of the wedges are rarely cylindrical. Instead, they display lateral variations and limits.

[3] A wealth of scientific studies has been dedicated to the understanding of the dynamics and mechanics of thrust wedges. In the early to middle 1980s, a series of influential papers has analytically described the feedback of the base dip angle of a sedimentary wedge, its internal and its basal strength on the resulting surface taper [Dahlen, 1984; 1990; Dahlen et al., 1984; Davis and Engelder, 1985; Davis et al., 1983]. The structural evolution of accretionary thrust wedges was then investigated by analogue models [Graveleau et al., 2012, and references therein], but the last decade has witnessed the usage of a growing number of numerical techniques [e.g., Buiter et al., 2006; Ruh et al., 2012; Simpson, 2009]. Both experimental approaches bear advantages. Analogue models are employing "real" materials, and the structures produced can be compared to those of natural examples. Different viscous and frictional materials can be utilized, and actual failure of the material generates shear zones. Numerical simulations, on the other hand, bear the advantage that parameters such as time, viscosity, brittle strength, and geometrical scale implemented into the system of equations can be rigorously scaled to large scale tectonic systems. Furthermore, numerical results provide direct and absolute values for strain and stress, and boundary conditions can be controlled throughout the whole simulation time.

[4] Numerical modeling of fold-and-thrust belts, where faulting occurs if stresses overcome the yield stress of brittle materials, needs accurate treatment of brittle/plastic rheology. Numerical modeling also requires a high resolution to produce spontaneously localizing, high strain rate shear bands narrow to the point that they can be compared to "faults." In the case of accretionary wedges and fold-and-thrust belts, this localization applies to the basal décollement and the various thrust flats and ramps, while respecting the high viscosity of the modeled, deforming sedimentary pile. Effective viscosity variations across narrow shear bands often range

over five orders of magnitude. This poses a tangible numerical challenge.

[5] Many geological problems, such as the influence of the strength of single and multiple décollements [Fillon et al., 2013; Ruh et al., 2012; Stockmal et al., 2007] or the effect of elasticity and viscosity of the décollement and overburden [Simpson, 2009] have been investigated using two-dimensional (2D) numerical models. A three-dimensional (3D) setup is needed to study the effects of lateral variations in any of the geometrical and/or mechanical parameters that control wedges. Although 3D numerical studies with plastic/brittle rheology exist [Allken et al., 2011; Braun et al., 2008; Gerya, 2010a; Popov and Sobolev, 2008; Zhu et al., 2009], few concern convergent thin-skinned thrust wedges. We present a 3D, high-resolution, fully staggered finite difference grid, marker in cell model for thin-skinned fold-and-thrust belts with a visco-brittle/plastic rheology. We use this model to understand the influence of pre-existing backstop offsets on the structural evolution of accretionary wedges and the role of basal frictional strength within these systems.

[6] We compare our 3D numerical results to the transfer/transform zone between the Zagros and the Makran, where the ~300 km long Minab-Zendan right lateral fault zone separates the Zagros foreland fold-and-thrust belt from the Makran accretionary wedge [Peyret et al., 2009; Regard et al., 2005; Smith et al., 2005]. Our aim is not to investigate the origin of this transfer zone, i.e., the cause of the recent offset in the actual backstop between the two wedge systems. We rather want to understand the effect of the existing transfer zone on the structural deformation and subsequent topography during ongoing shortening.

2. Numerical Model

2.1. Governing Equations

[7] We developed a 3D, high-resolution, fully staggered grid, finite difference, marker in cell model with a standard visco-brittle/plastic rheology and an efficient OpenMP-parallelized multigrid solver [Gerya, 2010b; Gerya and Yuen, 2007]. The mechanical model is built on the equations for conservation of mass assuming incompressibility (i.e., sediment compaction is neglected)

$$\frac{\partial u_i}{\partial x_i} = 0 \quad (1)$$

and the conservation of momentum, the Stokes equation

$$-\frac{\partial P}{\partial x_i} + \frac{\partial \tau_{ij}}{\partial x_j} = \rho g_i \quad (2)$$

where

$$\tau_{ij} = 2\eta \dot{\epsilon}_{ij} \quad (3)$$

and

$$\dot{\epsilon}_{ij} = \frac{1}{2} \left(\frac{\partial u_i}{\partial x_j} + \frac{\partial u_j}{\partial x_i} \right). \quad (4)$$

[8] P is dynamic pressure, i.e., mean stress, u_i the velocity ($u_1 = u_x$, $u_2 = u_y$, $u_3 = u_z$), x_i the spatial coordinates ($x_1 = x$, $x_2 = y$, $x_3 = z$), τ_{ij} the deviatoric stress tensor, ρ the density, g_i the gravitational acceleration ($g_1 = g_2 = 0$, $g_3 = 9.81$ m/s²), η the viscosity, and $\dot{\epsilon}_{ij}$ the strain rate tensor.

[9] If differential stresses exceed the yield stress, plastic failure follows the Drucker-Prager yield criterion with the plastic yield function F (equation (5)) depending on the second invariant of the stress tensor τ^{II} and the yield stress σ_y

$$F = \tau^{II} - \sigma_y \quad (5)$$

where

$$\tau^{II} = \sqrt{\frac{1}{2} \tau_{ij}^2} \quad (6)$$

and

$$\sigma_y = P \cdot \sin\varphi + C \cdot \cos\varphi \quad (7)$$

[10] C is cohesion and φ the friction angle of the material. Strain or strain-rate weakening [e.g., *Buiter et al.*, 2006] is not used in our model.

2.2. Numerical Implementation

[11] The governing equations given in the previous section are solved numerically by discretizing equation (3) in an implicit manner, using an efficient OpenMP-parallelized multigrid solver, fully parallel on 16 threads. We adopted a standard geodynamic modelling approach which uses an effective viscosity formulation for the numerical treatment of visco-brittle/plastic deformation [e.g., *Buiter et al.*, 2006; and reference therein]. Similarly to non-Newtonian (e.g., power-law) viscous rheology, effective viscosity for visco-brittle/plastic flows characterizes a local

ratio between the deviatoric stress and the strain rate (equation (3)). In places, where the plastic yielding condition is not reached the deformation is purely linear viscous in accordance to the assumed background rock viscosity. The rheological behavior of the model is initially purely linear viscous. If stresses locally exceed the yield stress ($F(\tau_{ij}, P, \varphi, C) > 0$), effective viscosities η are decreased depending on the second invariant of the strain rate tensor $\dot{\epsilon}^{II}$ and the yield stress σ_y until the maximum stresses are at the yield stress ($F = 0$), according to

$$\eta_{vp} = \frac{\sigma_y}{2\dot{\epsilon}^{II}} \quad (8)$$

where

$$\dot{\epsilon}^{II} = \sqrt{\frac{1}{2} \dot{\epsilon}_{ij}^2} \quad (9)$$

and η_{vp} is the effective viscosity corrected for plasticity.

[12] Direct plastic (Picard) iterations are simultaneous with time stepping. To ensure initial model convergence and proper initiation of shear bands, the first ~400 Picard iterations are computed with a very small time step (1 year), implying a negligible amount of model displacement. The following computational time steps are also relatively short (1000 years), which guaranties small material displacement per time step (<10 m) and ensures accurate treatment of plasticity and good convergence of the multigrid solver.

2.3. Initial Geometry and Material Parameters

[13] We present model setups with two different sizes for the finite Eulerian grid. The Eulerian grids are dimensioned in a way that account for different requirements: vertical thickening of the wedge, possible lateral structural changes throughout the evolving wedge and increasing length of the wedge while the wedge front migrates. A high-resolution grid is necessary to develop high strain rate shear bands sufficiently narrow to be comparable to natural fault systems. A first series of simulations had a perfectly cylindrical geometrical setup, i.e., a vertical, planar backstop formed by the Eulerian grid boundary. For these requirements, dimensions in x -, y -, z -directions are 150*50*15 km with a nodal resolution of 309*85*149, respectively. The resulting cell size in these models is 487*595.2*101.4 m in x -, y -, z -directions. Models with an initial offset of the backstop boundary have a size of 150*100*15 km in x -, y -, z -directions, respectively, including a 50 km

wide (y -direction) orthorhombic rigid body reaching into the model domain of the wedge. In these simulations, the backstop is represented by the Eulerian grid boundary from $y = 0 - 50$ km. From $y = 50 - 100$ km, the actual backstop boundary is offset by the length (x -direction) of the attached body (Figure 1). The nodal Eulerian grid resolution of these simulations is $309 \times 165 \times 149$ in x -, y -, z -directions, respectively. The resulting cell size in these models is $487 \times 609.8 \times 101.4$ m in x -, y -, z -directions. Lagrangian marker resolution of all simulations is two markers per cell in every direction. This setting results in a resolution of 7.6 million nodes with about 60 million Lagrangian markers for models with highest resolution.

[14] From bottom to top, the initial marker distribution defines a 500 m thick rigid plate at the bottom. Above this rigid plate, a 500 m thick décollement horizon with a frictional rheology soles a 5 km thick “sedimentary” sequence. The rest of the marker grid above the “sedimentary” sequence is defined as “sticky-air,” an approach that mimics a quasi-free surface between the model and the sticky-air [Crameri *et al.*, 2012; Gerya and Yuen, 2003; Schmeling *et al.*, 2008; Zaleski and Julien, 1992]. The roofing sticky-air layer has an initial thickness of 9 km (Figure 1). The low density (1 kg/m^3) and small viscosity ($10^{18} \text{ Pa}\cdot\text{s}$) of the air layer ensures sufficiently small normal stresses at the topography surface. The analytical prediction of the quality of the free-surface approach, given by Crameri *et al.* [2012; equations 7 and 18] is not directly applicable to our model setup because it was developed to test free-surface behavior

influenced by a gravity-driven viscous plume. Nevertheless, the main parameters of the equation are density, viscosity, and thickness of the sticky-air layer. Applying the equation to our setup yields very low quality factors $C_{max} (\ll 1)$, which fulfils the general condition for a traction free surface. Crameri *et al.* [2012] also tested the influence of numerical space and time resolution. A vertical grid resolution of ~ 100 m and time steps of 1000 years, as introduced in this study, are adequate to ensure a quasi-free surface [personal confirmation from Fabio Crameri].

[15] To investigate the structural evolution in function of the offset of the backstop front, three initial geometries have been introduced, differing in length of the rigid body L_B , i.e., backstop offset, in x -direction: $L_B = 20, 40, \text{ and } 80$ km. These promontories lie above the décollement horizon. Rigid backstop bodies have an initial thickness of 6500 m, looming 1.5 km above the “sedimentary” wedge sequence, and are therefore roofed by 7500 m of “sticky-air” (Figure 1). To simplify the discussion throughout this paper, we divide the model setup into two main domains: Domain A is defined by y -coordinates from 0 to 50 km, where no additional body is introduced. Domain B is the volume between y -coordinates 50 to 100 km, where the additional rigid body represents the backstop offset and promontory (Figure 1; top right).

[16] Material parameters of the different model elements are listed in Table 1. Every geometrical setup has been modeled with three décollement strengths, $\varphi_b = 5^\circ, 10^\circ, 15^\circ$.

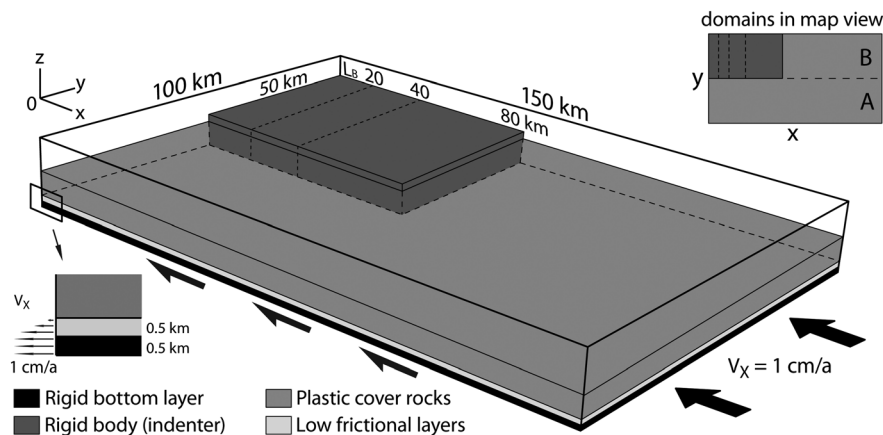


Figure 1. Model setup. From bottom to top: 500 m thick rigid plate (black), 500 m thick frictional décollement (light gray), 5 km thick sedimentary sequence (gray). Lowermost rigid plate (black) enters and exits the Eulerian grid. Dashed lines: three tested geometries (lengths 20, 40, 80 km) for a 50 km wide promontory (dark gray). Black arrows: Applied velocity boundary conditions. Top right: Definition of domain A (no promontory) and domain B (additional rigid body).

Table 1. Initial material parameters

Parameter	Description	Rigid basal plate	Décollement layer	Rock sequence	Rigid backstop	Sticky-air
φ	Friction angle (°)	-	5, 10, 15	30	-	-
C_0	Cohesion (MPa)	-	0.1	20	-	-
η	Initial viscosity (Pa·s)	1e23	1e23	1e23	1e23	1e18
η_{max}	Upper cutoff viscosity (Pa·s)	1e23	1e23	1e23	1e23	1e18
η_{min}	Lower cutoff viscosity (Pa·s)	1e23	1e18	1e18	1e23	1e18
ρ	Density (kg/m ³)	2400	2400	2400	2400	1

2.4. Boundary Conditions

[17] Instead of pushing the backstop over the weak décollement, boundary conditions are applied in a way similar to analogue sand box models where the bottom sheet is pulled out below a rigid backstop [e.g., *Konstantinovskaya and Malavieille, 2011*]. For this, a velocity of 1 cm/a is defined at the lower ($z = 0$ km) and frontal boundaries ($x = 150$ km; Figure 1). New Lagrangian marker layers coming in through the front side allow large deformation. The back side of the setup ($x = 0$ km) acts as backstop with a no-slip boundary condition. At the bottom, the 500 m thick rigid plate of high constant viscosity is included, which allows for a better stability of the multigrid solver at the lower model boundary. Between the bottom rigid plate and the “backstop,” the 500 m thick décollement undergoes simple shear (1 cm/a at $z = 500$ m to 0 cm/a at $z = 1000$ m; Figure 1). Both lateral boundary conditions (at $y = 0$ km and $y = 100$ km) are defined as free slip along the boundary planes. At the upper boundary, an upward velocity is applied. This leads to an exit of sticky-air markers of the same volume as the

material coming in at the front boundary to fulfill the conservation of volume.

2.5. Surface Process

[18] A 2D diffusive surface process is implemented to address sedimentation in piggy-back basin style depressions. The topography surface is treated as a boundary surface between “rocks” and sticky-air. The position of the surface between rock and sticky-air is calculated for every single vertical Eulerian grid line by using the nodal density. Densities of the markers defined as rock and sticky-air are $\rho_{rock} = 2400$ kg/m³ and $\rho_{sticky-air} = 1$ kg/m³, respectively. The density of Lagrangian markers is averaged harmonically on the nodes. This averaging results in a density column that fades over four nodes from ρ_{rock} to $\rho_{sticky-air}$ (Figure 2a; node 110 to 113). The elevation of the sticky-air/rock interface is placed above the highest node that has a density larger than the average ($\rho_{surface}$):

$$\rho_{surface} = \frac{\rho_{rock} + \rho_{sticky-air}}{2} = 1200.5 \text{ kg/m}^3 \quad (11)$$

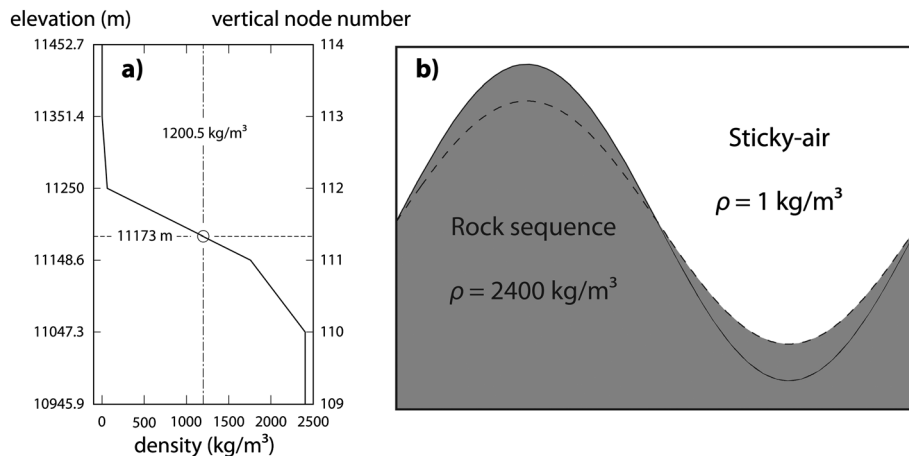


Figure 2. Diffusive surface process. a) Density change at the sticky-air/rock interface along a random vertical nodal grid line. Solid line: density along a node column. Dot-dashed line: average of sticky-air and rock density. Dashed line: elevation, where the interpolated density is equal to the sticky-air/rock density average. b) Application of the diffusive process. Solid line: interface before the diffusion. Dashed line: interface after the diffusion. Grey area: rock sequence after surface process application. White area: sticky-air after surface process application.

[19] In the example density column (Figure 2a), it is node number 111, at 11148.6 m elevation. A linear interpolation of density at node number 111 to density at the node number 112 (which is the first node with a density below $\rho_{surface}$, above node 111) crosses the average density $\rho_{surface}$. The elevation at which the density interpolation crosses $\rho_{surface}$ represents the elevation of the adjusted surface (Figure 2a). This procedure yields an “exact” topography independent of the nodal resolution. To simulate surface process, the topography surface is diffused at every time step depending on its local 2D curvature:

$$\frac{\partial h_s}{\partial t} = \kappa \cdot \frac{\partial^2 h_s}{\partial x_i^2} \quad (12)$$

where κ is the diffusion constant, h_s the surface topography, and x_i the spatial coordinates ($x_1 = x$, $x_2 = y$). The diffusion constant is $\kappa = 10^{-9}$ m/s² in all simulations presented here. The topography diffusion equation was solved implicitly on one thread using the direct solver PARDISO [Schenk and Gartner, 2004; 2006].

[20] To address a depositional process without erosion, markers with a sticky-air rheology below the updated surface transmute to rock rheology. Markers with rock rheology above the updated surface remain unchanged (Figure 2b). The present study does not aim investigating the influence of sedimentation and erosion on the evolution of thrust wedges. We refer to the wealth of publications investigating feedbacks between surface processes and the internal deformation of such systems [e.g., *Beaumont et al.*, 1992; *Hilley and Strecker*, 2004; *Koons*, 1990]. The intensity of topography diffusion process in our model is low and mainly aims to preclude overthrusting of low-viscosity sticky-air markers at the model surface, which may produce nonphysical entering of the sticky-air into spontaneously forming thrust zones.

3. The Critical Wedge Theory

[21] In the late 1970s and early 1980s, several publications [*Chapple*, 1978; *Dahlen*, 1984; 1990; *Dahlen et al.*, 1984; *Davis and Engelder*, 1985; *Davis et al.*, 1983] compared the evolution of an accretionary wedge to a pile of sand pushed by a bulldozer. For a frictional décollement, as it is introduced in our model setup, the analytical solution predicts a minimum and a maximum critical total taper (defined by the surface α + base β angle), depending on the internal strength of the wedge

material, the strength of the décollement and the base dip angle β . In contrast, the analytical solutions of critical wedges overlying a viscous décollement depend also on wedge density, thickness, and compression velocity. This dependence is due to the resistance to shear in a purely viscous décollement, which depends on the velocity difference between its bottom and top surfaces. The shear resistance in the linear viscous case is independent of the thickness of the overlying sequence. In theory, whatever the type of décollement, the rear of the developing wedge thickens by thrusting until the critical minimum taper is reached, which sets the wedge in a stable mode. As long as the total taper remains above its critical minimum, the wedge is sliding along its décollement and is growing by frontal accretion of new material in an in-sequence style of thrusting. If the taper angle exceeds the maximum critical taper, it will be lowered by normal faults.

[22] The critical wedge theory exists for noncohesive as well as for cohesive cases. Taking into account the effect of cohesion, the wedge surface becomes concave if the décollement is planar [*Dahlen et al.*, 1984]. *Simpson* [2011; Figure 15] argued that cohesion strength actually has a negligible influence on the shape of brittle wedges. This argument is disputable, *Nilfouroushan et al.* [2012] having shown that the structural evolution of numerical wedges is actually sensitive to changes in cohesion.

[23] The analytical critical taper theory assumes that the whole wedge is at a critical stress state throughout. Time is irrelevant for the analytical solution, which represents only the state when the taper increases or decreases while stresses are perfectly distributed. It is obvious that a mechanical brittle/plastic wedge, whether analogue or numerical, is not at failure throughout [*Simpson*, 2011]. If the taper is below the critical minimum, the wedge fails and activates thrusts at its rear to increase its surface slope. If it is in a stable mode, above the critical minimum, the wedge does not deform internally and is accreting new material at the front, consequentially decreasing its critical taper. Analogue sandbox models [*Davis et al.*, 1983] and 2D numerical models [*Ruh et al.*, 2012] demonstrated that tapers of compressional brittle/plastic wedges are leveling toward the minimum critical taper defined by the critical wedge theory.

3.1. Influence of Basal Friction

[24] In this work, we are investigating whether the noncohesive critical wedge theory can also be

applied to noncylindrical numerical wedge models. The analytically derived critical surface taper angles are plotted against the décollement angle for a wedge with an internal friction angle of $\varphi = 30^\circ$ and basal friction angles of $\varphi_b = 5^\circ, 10^\circ,$ and 15° (Figure 3a).

[25] Basal friction affects the shape and the structural behavior of a thrust wedge. The theory of noncohesive critical wedges provides the expected surface slope (α), the angle between the maximum principal stress σ_1 and the base ψ_b , and the angle

between the maximum principal stress σ_1 and the top of the wedge ψ_0 [Dahlen, 1984; Davis et al., 1983]:

$$\alpha + \beta = \frac{\tan \varphi_b + \beta}{1 + K} \quad (13)$$

where $K \approx \frac{\sin \varphi}{1 - \sin \varphi} + \frac{\sin^2 \varphi_b + \cos \varphi_b (\sin^2 \varphi - \sin^2 \varphi_b)^{1/2}}{\cos^2 \varphi_b - \cos \varphi_b (\sin^2 \varphi - \sin^2 \varphi_b)^{1/2}}$, φ and φ_b the internal and basal friction angles of the wedge and β the slope of the wedge base.

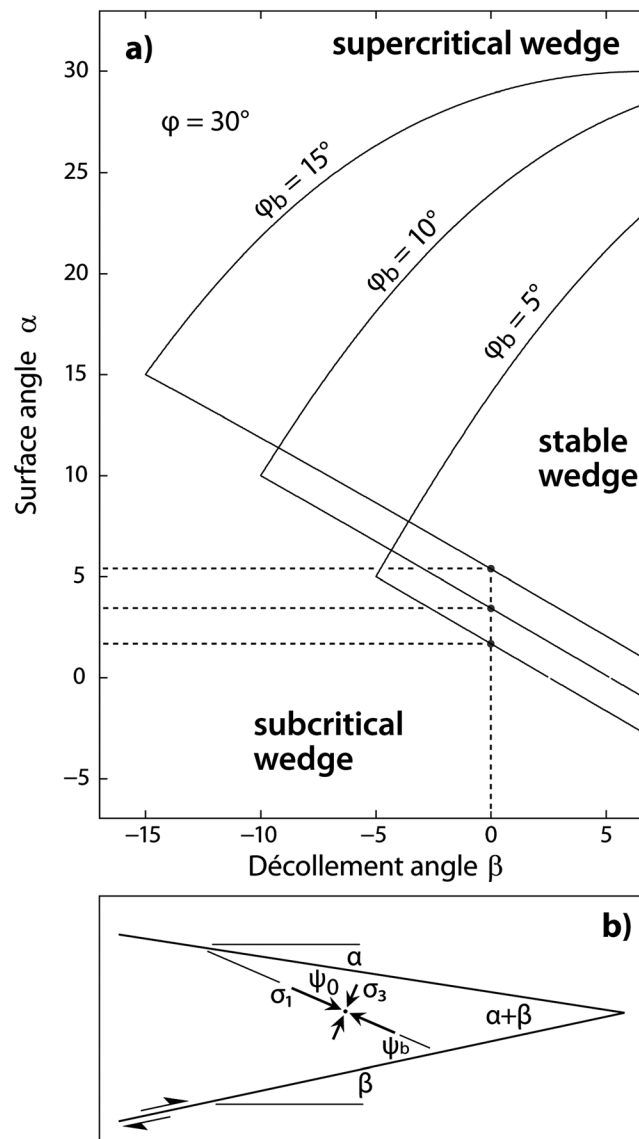


Figure 3. a) Flounder diagrams of the stability of frictional wedges with an internal friction angle $\varphi = 30^\circ$ and basal friction angles φ_b of $5^\circ, 10^\circ,$ and 15° [Dahlen, 1984] relating minimal and maximal critical tapers to dip angle β of the basal décollement (points within the flounder-shaped area indicate a stable wedge, points outside are unstable wedges). Dashed lines: minimum critical surface taper angles for the three cases with a horizontal basal décollement ($\beta = 0^\circ$). b) Definition of angles $\alpha, \beta, \psi_b, \psi_0$ in a critical wedge and related principal stresses σ_1, σ_3 in two dimensions.

$$\psi_b = \frac{1}{2} \arcsin\left(\frac{\sin\varphi_b}{\sin\varphi}\right) - \frac{1}{2}\varphi_b \quad (14)$$

$$\psi_0 = \frac{1}{2} \arcsin\left(\frac{\sin\alpha}{\sin\varphi}\right) - \frac{1}{2}\alpha \quad (15)$$

[26] Two major points were raised from previous analogue and numerical studies: i) the taper increases with increasing basal friction, which leads to a narrower wedge [Burbidge and Braun, 2002; Davis et al., 1983; Nilforoushan et al., 2008]; and ii) with increasing basal friction, principal stresses plunge with higher angles toward the wedge toe, which leads to steeper back thrusts and flatter frontward-verging thrusts [Huiqi et al., 1992.; Mulugeta, 1988; Ruh et al., 2012].

[27] The dip angles of frontward- and backward-verging thrusts can be predicted from the angle ψ_b between the wedge basis and the maximum principle stress. It is known that the angle between the inclination of shear bands and the maximum principal stress varies between the Roscoe angle θ_R , the Coulomb angle θ_C , and the Arthur angle θ_A [Arthur et al., 1977; Coulomb, 1773; Roscoe, 1970]:

$$\theta_R = 45 - \frac{\Psi}{2} \quad (16)$$

$$\theta_C = 45 - \frac{\varphi}{2} \quad (17)$$

$$\theta_A = 45 - \frac{\varphi + \Psi}{4} \quad (18)$$

where Ψ is the dilation angle [Roscoe, 1970], which in our simulations is 0. Angles outside the Roscoe-Coulomb range are not expected to occur in numerical models [Kaus, 2010]. The different angles of shear band plane dips (θ_R , θ_A , θ_C) can be rotated by

the predicted angle ψ_b to calculate the expected dips of frontward and backward verging shear band.

[28] Here, we want to compare our numerical results to the critical wedge theory in terms of surface slope and internal stress directions. Therefore, values for the expected taper, stress orientation and expected shear band plane dips after Roscoe, Arthur, and Coulomb are listed in Table 2 and illustrated in Figure 3b.

4. Results

[29] Twelve simulations are presented. Three simulations without backstop offset allow investigating the influence of basal friction ($\varphi_b = 5^\circ, 10^\circ, 15^\circ$). These three models have a width of $y = 50$ km and have been run for 7 Ma numerical time. Deformation initiated along the singularity line, where the rigid plate is pulled out below the backstop. Due to their simple geometry, these models developed cylindrical structures that compare well, in section, with 2D simulations.

[30] In addition to every cylindrical basal strength setup, simulations including three initial backstop offsets (transfer zones defined by adding rigid bodies; Figure 1) have been carried out. In the following, we refer to the rigid body as promontory because it is a strong backstop reaching into the wedge material. Simulations with a basal friction angle of $\varphi_b = 5^\circ$ were running for 5 Ma, models with larger basal friction ($\varphi_b = 10^\circ, 15^\circ$) for 6 Ma.

4.1. Different Basal Déollement Strength

[31] Deformation of the compressed wedge, inferred from plotted Lagrangian markers, and the strain rate are illustrated for the three basal strengths after

Table 2. Analytical values predicted and derived from the critical wedge theory for the three cylindrical model setups (Figures 4 and 5)

Parameter	Description	Model 1	Model 2	Model 3
φ	Internal friction ($^\circ$)	30	30	30
φ_b	Basal friction ($^\circ$)	5	10	15
β	Base angle ($^\circ$)	0	0	0
α	Surface slope ($^\circ$)	1.7	3.4	5.3
ψ_b	Angle between β and σ_1 ($^\circ$)	2.5	5.2	8.1
ψ_0	Angle between α and σ_1 ($^\circ$)	0.8	1.7	2.7
θ_{RF}	Roscoe angle for frontward thrust ($^\circ$)	42.5	39.8	36.9
θ_{RB}	Roscoe angle for backward thrust ($^\circ$)	47.5	50.2	53.1
θ_{CF}	Coulomb angle for frontward thrust ($^\circ$)	27.5	24.8	21.9
θ_{CB}	Coulomb angle for backward thrust ($^\circ$)	32.5	35.2	38.1
θ_{AF}	Arthur angle for frontward thrust ($^\circ$)	35.0	32.3	29.4
θ_{AB}	Arthur angle for backward thrust ($^\circ$)	40.0	42.7	45.6

7 Ma with the cylindrical model setup (Figure 4). Wedge tapers are narrower and have a steeper surface slope with increasing basal strength. The spatial distribution of markers transformed into new sediment indicates a piggyback style of transport with sedimentation taking place only at local troughs. Both the deformed strata and strain rate plots (Figure 4) indicate an almost perfectly cylindrical deformation style of the wedge, independent of the basal strength (small irregularities along the y -axis are due to random marker distribution). This highlights the robustness of the numerical code and negates any lateral boundary effects. The second invariant of the strain rate tensor shows that the wedge material is deforming in a mainly brittle/plastic manner. Narrow, high strain rate shear bands delineate thrust faults. Strain rate values within the décollement indicate whether it is active.

[32] If the décollement has a low frictional strength ($\varphi_b = 5^\circ$), a wide wedge with low maximum elevation develops (Figure 4a). The wedge front migrates toe-ward before a notable offset appears along shear bands. Therefore, it is difficult to identify thrusts with the plotted deformed strata. Frontal accretion takes place through conjugate, high strain rate shear bands whose symmetry is favored by the almost horizontal main principal stress direction. The result is a wedge with a flat surface slope. Out-of-sequence thrusting takes place at the rear while failure is active at the toe of the wedge. This indicates that out-of-sequence thrusts act as a buffer to maintain the taper at its critical minimal value.

[33] For higher basal décollement strengths ($\varphi_b = 10^\circ, 15^\circ$), the wedges are narrower and display steeper surface slopes (Figures 4b and 4c). Strain rate plots

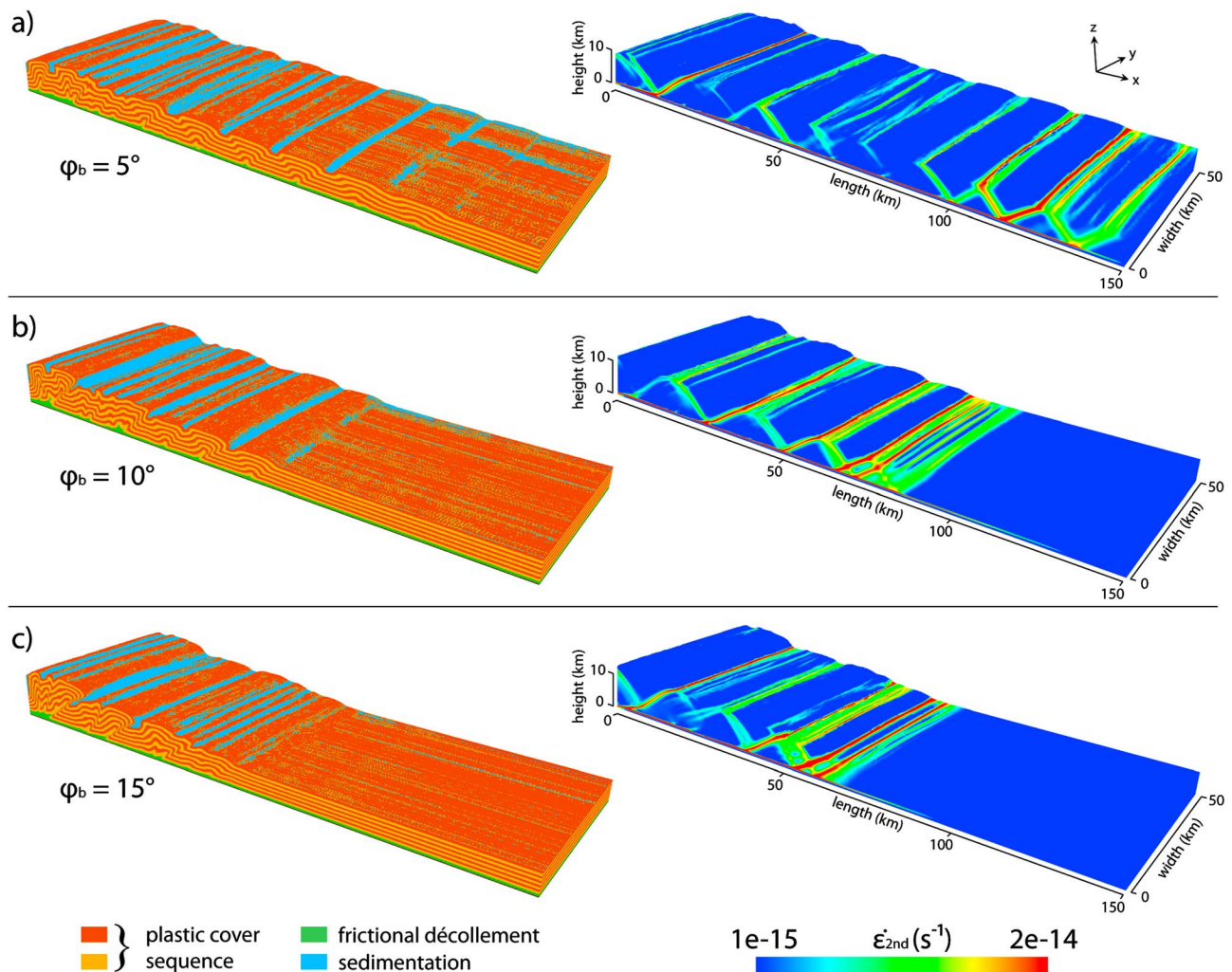


Figure 4. Cylindrical simulations after 7 Ma run time, i.e., a total shortening of 70 km. Internal friction angle of $\varphi = 30^\circ$, basal friction angles of a) $\varphi_b = 5^\circ$, b) 10° , and c) 15° . Left: Lagrangian markers indicating wedge deformation. Right: Second invariant of the strain rate tensor.

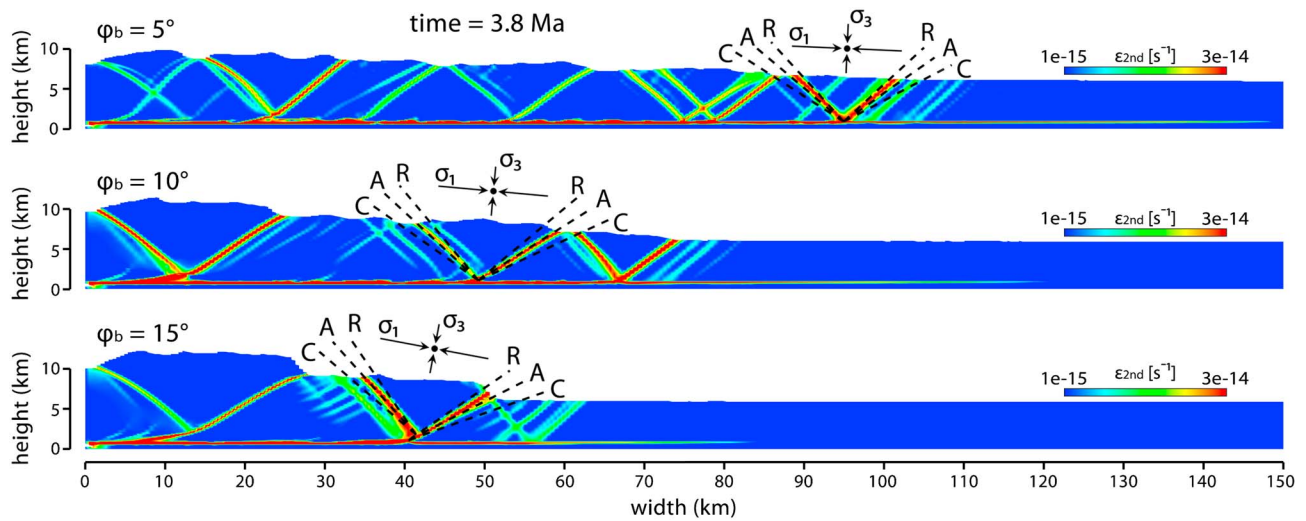


Figure 5. Profiles of the second invariant of the strain rate tensor at 25 km width of the three simulations illustrated in Figure (4). Black dashed lines indicate forward and backward verging Roscoe (R), Arthur (A), and Coulomb (C) angles. The rake of principal stress orientations, σ_1 and σ_3 , and the dip of R, A, and C angles are listed in Table 2 for each model.

show two forward-verging thrusts very close to each other at the front of the wedges (Figures 4b and 4c). Accretion of new material mainly produces thrusts verging toward the wedge front and minor shortening due to backthrusting. This is due to the increased plunge of stress directions within the wedge body for higher basal strength (Figures 3b and 5). Analytically derived stress directions (equations (13), (15)–(17)) within a frictional wedge are compared to the orientation of shear band planes (Figure 5). 2D numerical models have shown that thrusts in compressional wedges tend to follow Coulomb orientations with respect to the main compressional stress direction [Ruh et al., 2012]. In the present 3D modeling, high strain rate shear bands are close to the Arthur angle, sporadically tending toward the Roscoe angle (Figures 5a and 5c). In general, simulations coincide with the analytical theory and the principal compression direction is increasingly steep toward the wedge toe with increasing basal strength. A consequence is that developing thrust ramps dip shallower and back thrusts steeper than in wedges with low basal friction.

[34] Snapshots of the profile at $y = 25$ km (Figure 6) of the simulation with a basal friction angle of $\varphi_b = 15^\circ$ (Figure 4c) show that deformation initiates at the rear of the model. The deformation front migrates through time away from the rear by forming in-sequence, forward verging thrust sheets. Sedimentary basins are formed in a piggy-back manner on top of rotating thrust sheets. Material is also deposited in front of active thrusts. During horizontal growth of the wedge due to frontal accretion, active

out-of-sequence thrusting deforms the rear part of the wedge. Through time, these formerly active, forward-verging and out-of-sequence thrusts are deactivated and rotate. This can be observed for the first thrust at the very back of the model (Figure 6). After 1 Ma, it dips $\sim 45^\circ$ toward the backstop. After 7 Ma, it is almost vertical.

[35] The surface slopes have been calculated by linear regression of all nodal surface elevations in a profile in x -direction at $y = 25$ km (Figure 7b). Another way of measuring the surface slope is to connect valleys (troughs in the surface line; Stockmal et al. [2007]). For the linear regression, only surface elevations 100 m higher than their initial value have been considered to neglect the flat fore-wedge that has not yet been incorporated into the wedge. At the beginning (~ 0.25 Ma), all slopes are negative. This is due to the activation of the first forward verging thrust. Then, they show very high tapers (~ 0.8 Ma), which result from the fact that only one or two thrust sheets construct the surface slope of the still narrow taper (e.g., Figure 6; at 1 Ma). The total tapers of simulations with a frictional strength $\varphi_b < 15^\circ$ reach their critical minimum at around 3 Ma. Then, out-of-sequence thrusts keep the taper in the stable mode. At 7 Ma run time, all simulations produced stable wedges and therefore accrete new material at their front.

[36] Knowing the expected slope and the incoming material flux, one can predict the length (x -direction) of the evolving wedge. All incoming rock volume V_I must be incorporated into the wedge and therefore

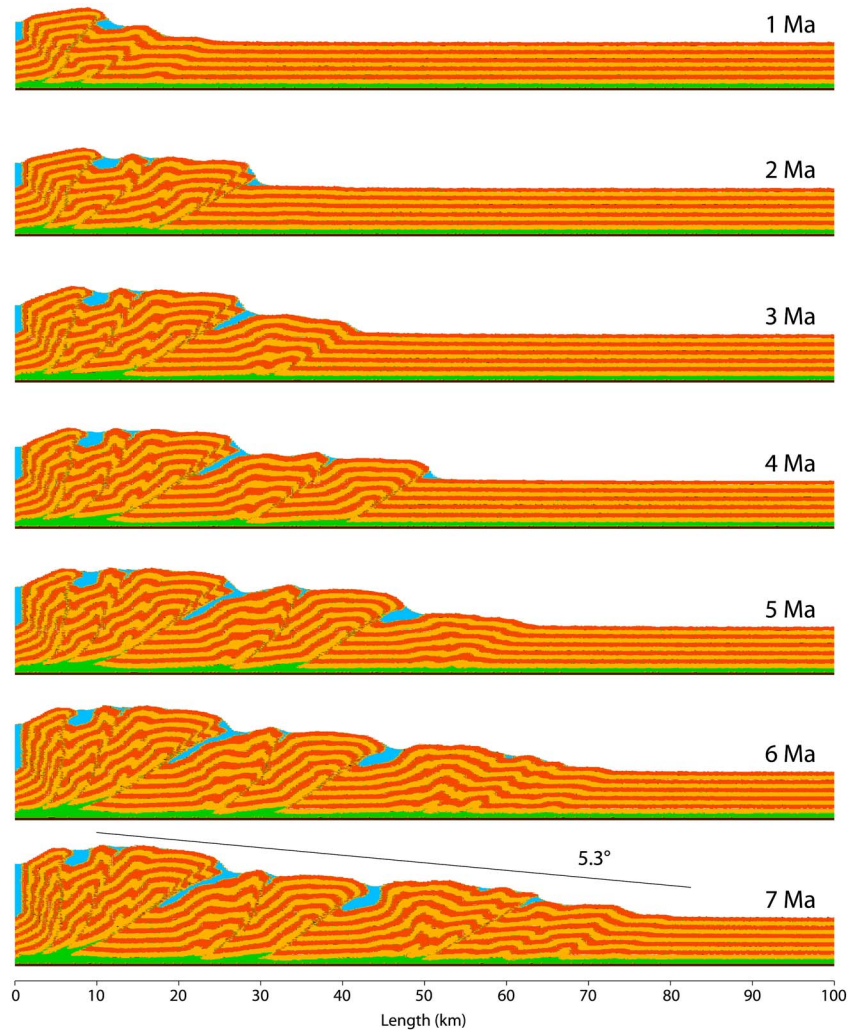


Figure 6. Temporal evolution of a brittle wedge (orange and brown, equal property layers) overlying a horizontal frictional décollement (green) at 25 km (y -direction) from the model side boundaries of the simulation with $\varphi = 30^\circ$ and $\varphi_b = 15^\circ$ (Figure 4c). Note in-sequence thrusting and wedge thickening due to out-of-sequence thrusting at the rear. Blue: new sediments deposited on the back limbs of fault anticlines. Solid line: analytically derived minimum critical taper. No vertical exaggeration.

be equal to the volume situated above the initially flat material (Figure 7a). V_I can be calculated from the thickness of the incoming pile H , the velocity v_x and time t according to

$$V_I = H \cdot v_x \cdot t \quad (19)$$

[37] The expected volume of the wedge above its initial level V_W depends on the analytical taper angle α and the wedge length in x -direction L_W (the horizontal distance from the backstop to the frontal thrust)

$$V_W = \frac{L_W^2 \cdot \tan \alpha}{2} \quad (20)$$

[38] Since V_W and V_I must be equal, equations (19) and (20) can be simplified and solved for the expected length L_W

$$L_W = \sqrt{\frac{2 \cdot H \cdot v_x \cdot t}{\tan \alpha}} \quad (21)$$

[39] In Figure 7c, the analytically derived L_W is plotted against time for the three considered cases ($\varphi_b = 5^\circ, 10^\circ, 15^\circ$). As previously seen, wedges with higher basal friction produce narrower tapers with steeper surface. The analytical wedge lengths match the numerically modeled wedges, especially for higher basal friction. For the low basal friction case ($\varphi_b = 5^\circ$), the fit between the analytical and

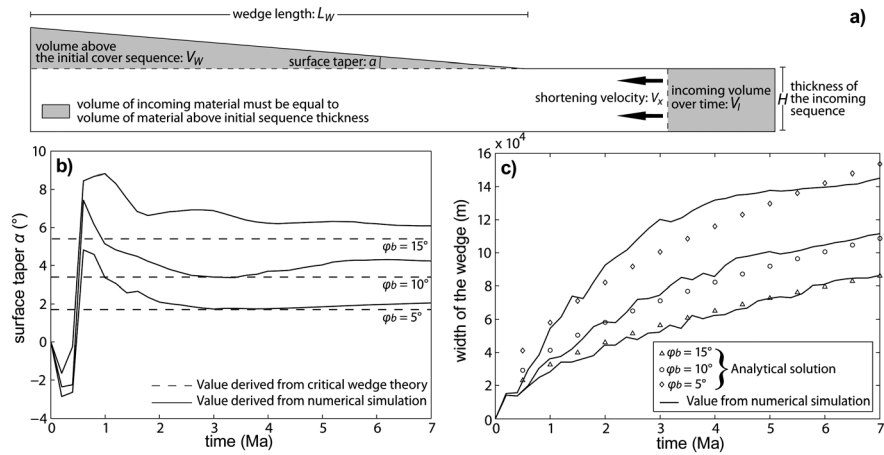


Figure 7. Analytical test of the numerical results. a) Profile sketch of a wedge. Grey: incoming volume (V_I) is equal to volume above initial level of the sequence (V_W). b) Temporal evolution of surface tapers of perfectly cylindrical simulations according to their basal frictional strength (Figure 4). Full lines: numerical results. Dashed lines: analytically derived minimum critical tapers. c) Temporal evolution of the wedge lengths (x -direction). Full lines: numerical results. Symbols: time-dependent analytically derived wedge lengths.

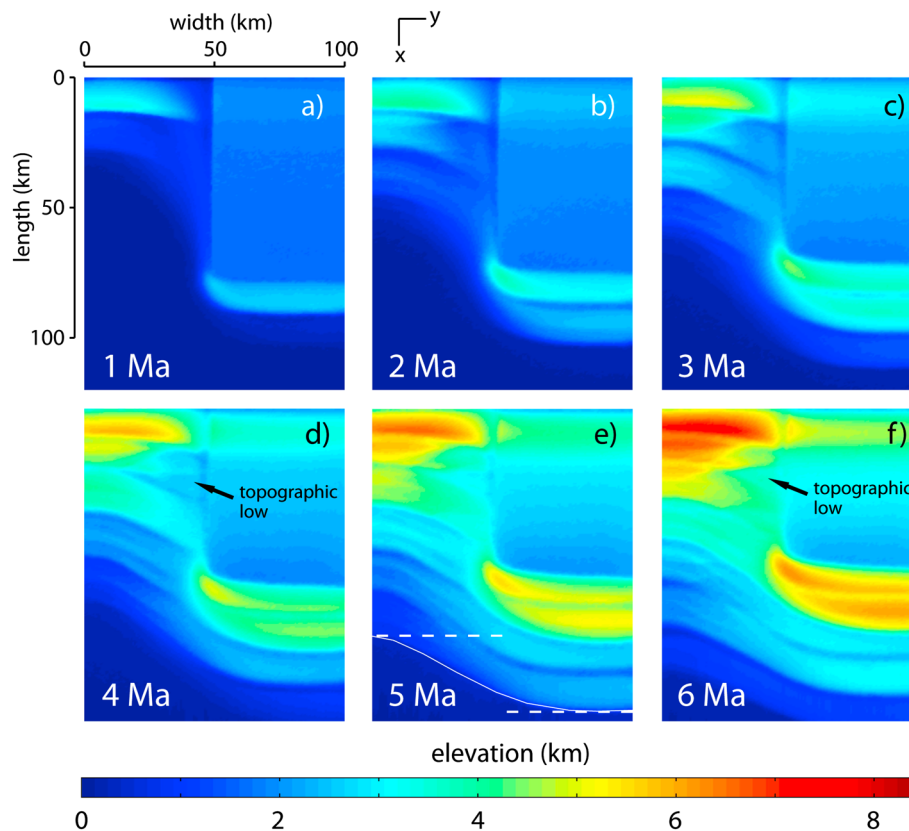


Figure 8. Map view of temporal evolution of a compressional wedge with a basal friction angle of $\varphi_b = 10^\circ$ and a backstop offset of $L_B = 80$ km. a) Elevated quadrangle in the right top indicates position of the promontory. d) Black arrow points to topographic low next to the promontory. e) Dashed lines: position of the frontal thrust at the lateral boundaries ($y = 0$ km, $y = 100$ km). Solid line: orientation of the frontal thrust. 1 Ma = 10 km of shortening.

the numerical solution is not as accurate as for the stronger décollement simulations. A reason could be that deformation is reaching the box boundary ($x = 150$ km) of this simulation at about 7 Ma.

4.2. Temporal Evolution of Models with a Backstop Offset

[40] In the following part, the model with a basal friction angle of $\varphi_b = 10^\circ$ and a backstop offset of $L_B = 80$ km is described to illustrate the evolution of a thrust wedge influenced by a predefined backstop promontory and lateral transfer zone. As already mentioned, we refer to the wedge part pushed by the indenting promontory as “domain B,” and to the wedge growing in front of the Eulerian grid boundary as the “domain A.” The promontory is clearly visible by its initially higher topography in contrast to the plastic sequence. The first thrust sheet develops along the backstop in domain A and at the front of the promontory in domain B (Figure 8a). The thrust sheet pushed by the promontory (domain B) is not linked to that formed in domain A. After 2 Ma, a second, in-sequence thrust develops in domain B, bending and fading out toward the transfer zone (Figure 8b). At the same time, domain A of the wedge already exhibits three thrusts, indicating that this part of the

wedge is growing faster in x -direction (convergence direction) than domain B, i.e., strain is more distributed. In domain A, the thrusts do not develop perfectly cylindrical, i.e., orthogonal to the bulk shortening direction. Due to connection of the thrust sheets with the promontory side, shortening is not provided by large fault offsets along the thrusts (Figure 8c). After 4 Ma, a topographic low is detectable along the transfer, lateral boundary of the promontory in domain A, in front of the first thrust sheet (Figure 8d). After 5 Ma, the maximal elevation at the rear of the wedge is larger in domain A than in domain B (Figure 8e). Furthermore, the frontal thrust, though still curved, is connected over the whole width (y -direction) of the model. The offset of the wedge front at the lateral boundaries ($y = 0$ km and $y = 100$ km) is smaller (30 km) in the x -direction than the initial backstop offset (80 km; Figure 8e). The topographic low, which started to develop at ca. 4 Ma, is significant at 6 Ma. This topographic low develops because the wedge in domain A is strongly noncylindrical (Figure 8f). Whereas the first thrust fault at the rear develops throughout the whole domain A, the second and third ones are less wide (y -direction). This forms a triangular (map view) elevated zone bordering the relative topographic low (Figure 8f).

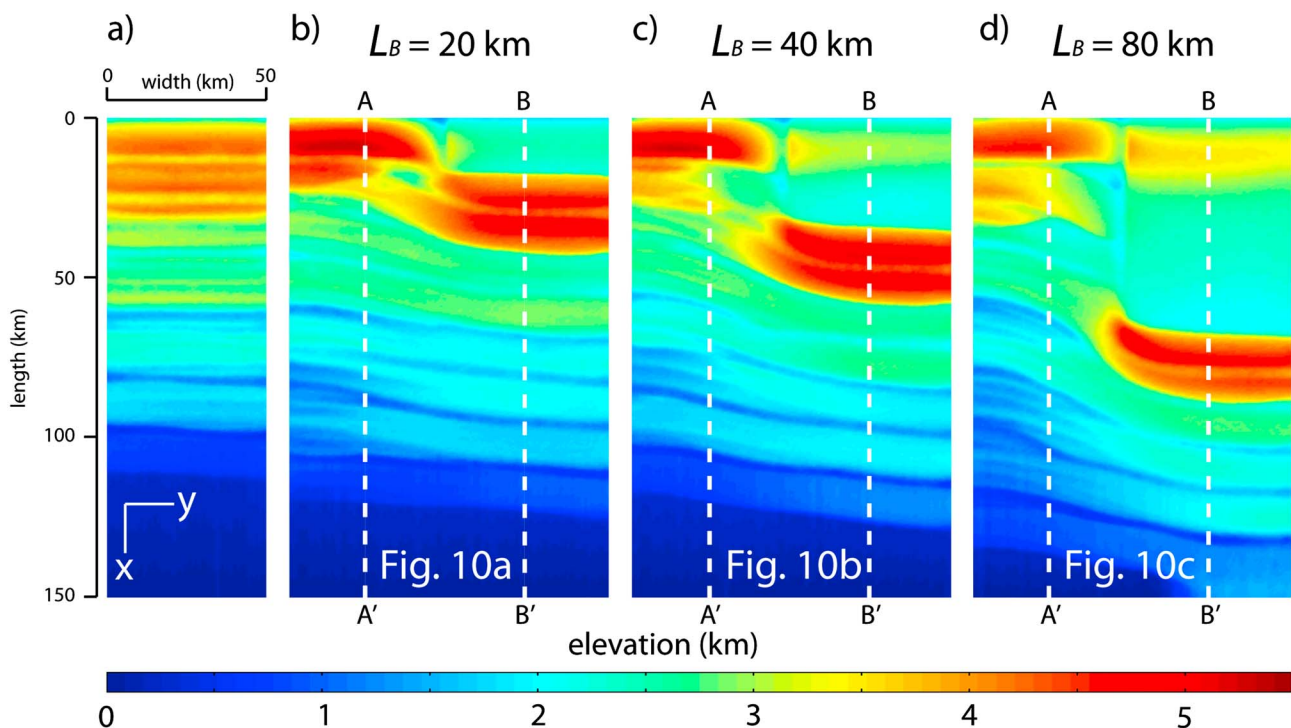


Figure 9. Topography of simulations with a basal friction angle of $\varphi_b = 5^\circ$ at 5 Ma run time. a) No promontory. b) $L_B = 20$ km. c) $L_B = 40$ km. d) $L_B = 80$ km. White dashed lines: position of slices in Figure 10.

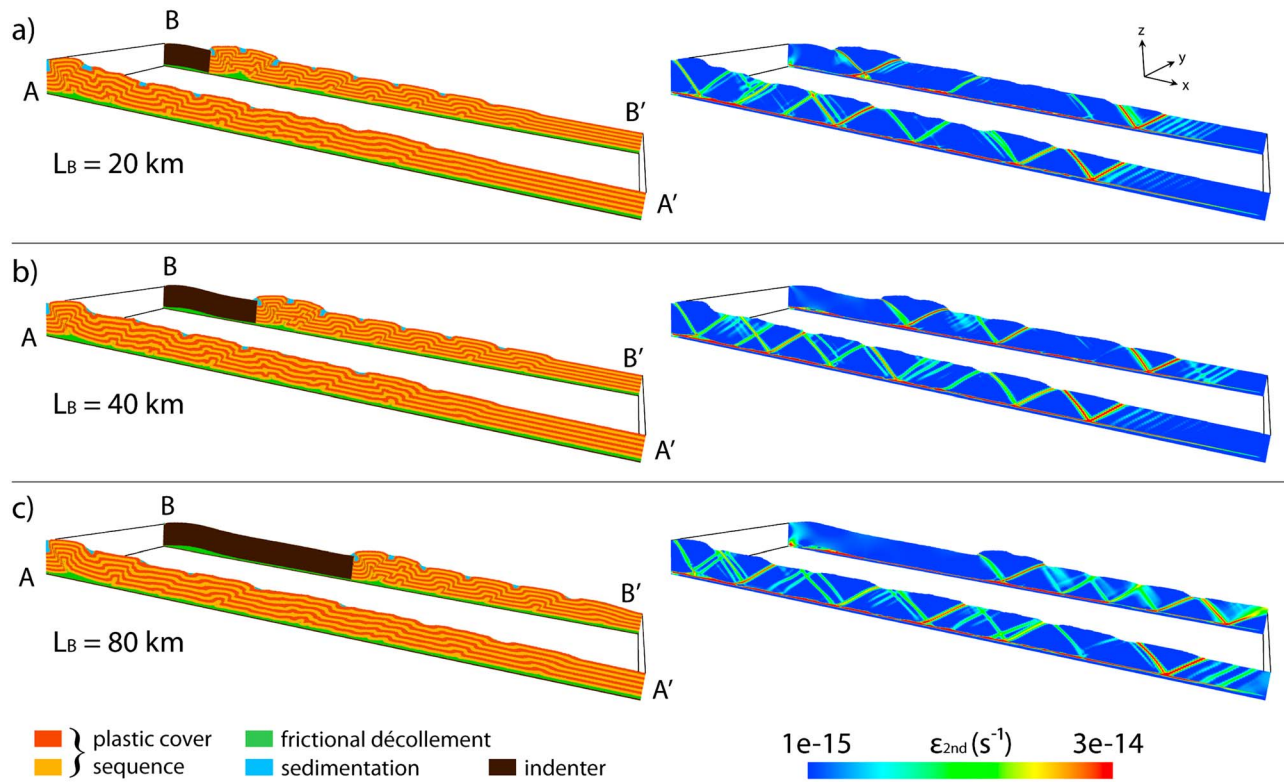


Figure 10. Slices showing wedge deformation inferred from Lagrangian marker grid (left) and second invariant of the strain rate tensor (right) for simulations with a basal friction of $\varphi_b = 5^\circ$ at 5 Ma run time.. a) $L_B = 20$ km, b) $L_B = 40$ km c) $L_B = 80$ km. Location of the slices is indicated in Figure 9.

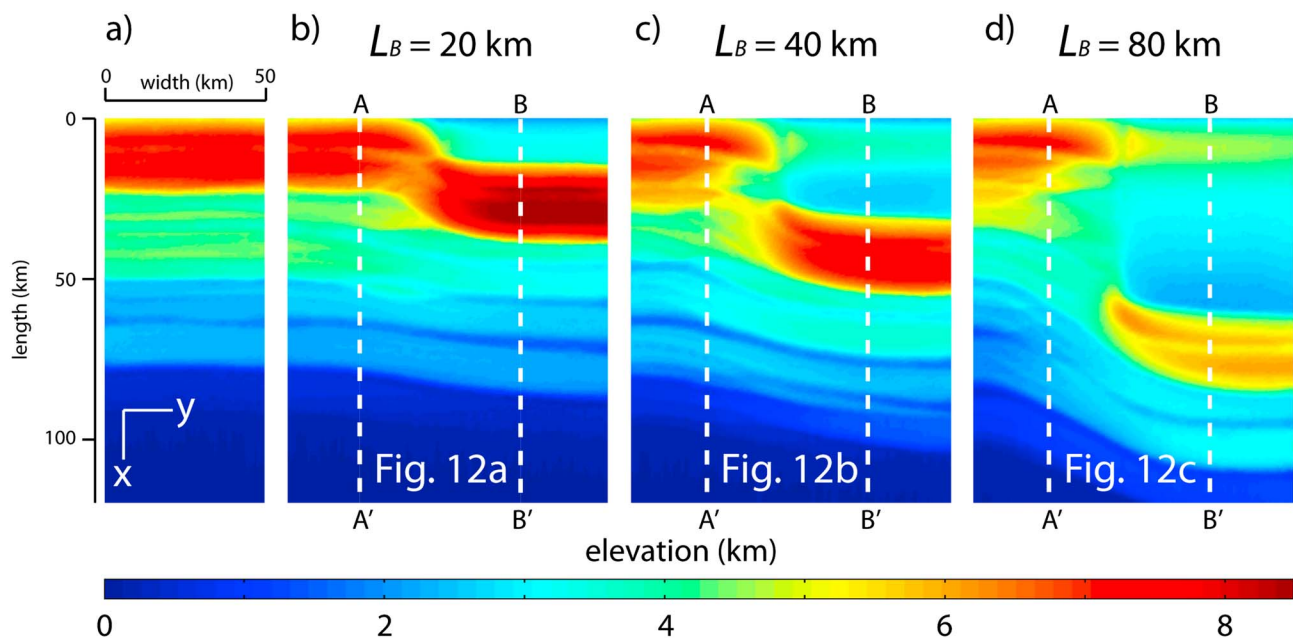


Figure 11. Topography of simulations with a basal friction angle of $\varphi_b = 10^\circ$ at 6 Ma run time. a) No promontory. b) $L_B = 20$ km. c) $L_B = 40$ km. d) $L_B = 80$ km. White dashed lines: position of slices in Figure 12.

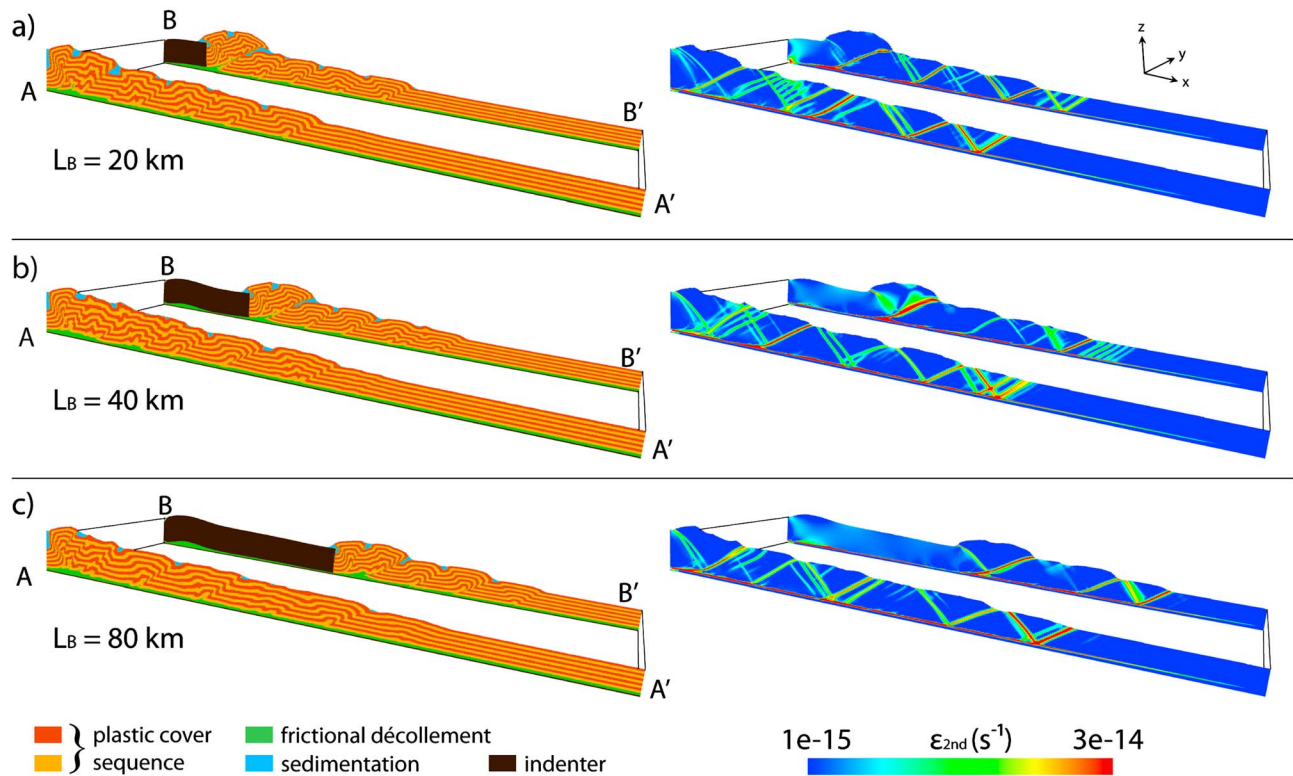


Figure 12. Slices showing wedge deformation inferred from Lagrangian marker grid (left) and second invariant of the strain rate tensor (right) for simulations with a basal friction of $\varphi_b = 10^\circ$ at 6 Ma run time. a) $L_B = 20$ km, b) $L_B = 40$ km c) $L_B = 80$ km. Location of the slices is indicated in Figure 11.

4.3. Influence of Backstop Offset L_B

[41] The influence of the backstop offset L_B is illustrated by plotting the surface topography in map view for all models at their final stage (Figures 9, 11 and 13). To illustrate the mechanics of these models with an induced transfer zone, slices at $y = 25$ km and $y = 75$ km show material phases and the second invariant of the strain rate

tensor for the different backstop offsets, according to their basal strength (Figures 10, 12 and 14).

4.3.1. Low Basal Friction ($\varphi_b = 5^\circ$)

[42] Models with different backstop offsets and a basal friction angle of $\varphi_b = 5^\circ$ are compared to their cylindrical equivalent at 5 Ma run time (Figure 9).

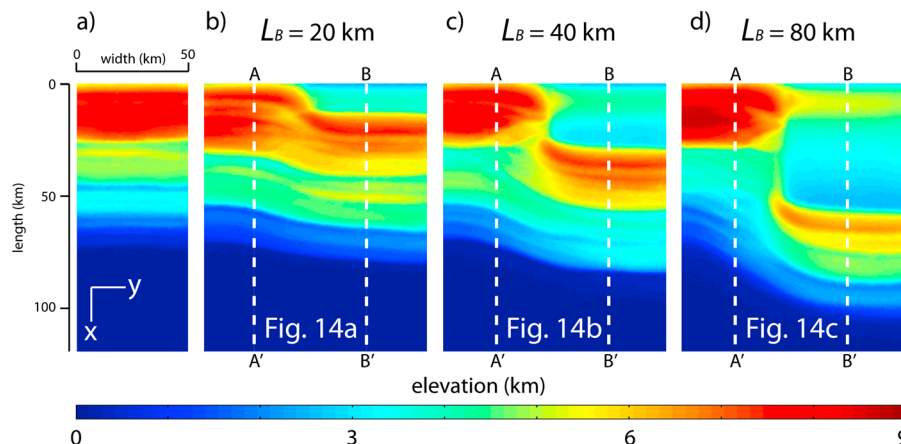


Figure 13. Topography of simulations with a basal friction angle of $\varphi_b = 15^\circ$ at 6 Ma run time. a) No promontory. b) $L_B = 20$ km. c) $L_B = 40$ km. d) $L_B = 80$ km. White dashed lines: position of slices in Figure 14.

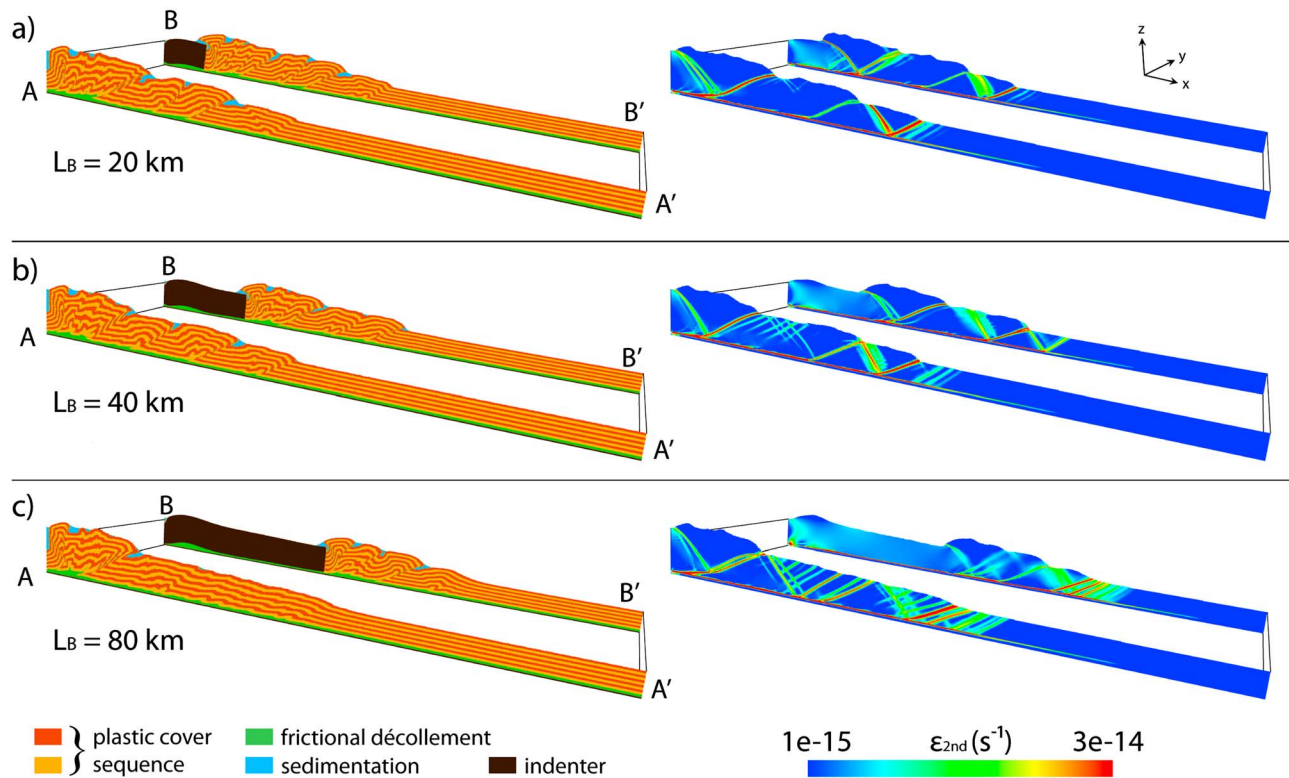


Figure 14. Slices showing wedge deformation inferred from Lagrangian marker grid (left) and second invariant of the strain rate tensor (right) for simulations with a basal friction of $\varphi_b = 15^\circ$ at 6 Ma run time. a) $L_B = 20$ km, b) $L_B = 40$ km c) $L_B = 80$ km. Location of the slices is indicated in Figure 13.

Elevation of the cylindrical model is maximal at the rear, reaching ~ 4.5 km higher than the initial surface of the sedimentary sequence (Figure 9a). All models with a backstop offset show higher maximal elevation (Figures 9b–9d). Maximal elevations of all modeled wedges with a low basal friction are similar in domains A and B, reaching 5 to 5.5 km higher than the initial surface. In the model wedge with a backstop offset of $L_B = 20$ km, the 5 Ma

frontal thrust is nearly linear and orthogonal to the bulk shortening direction (Figure 9b). The curvature of the frontal thrust and the thrust sheets around the promontory corner is tighter with longer backstop offsets ($L_B = 40$ and 80 km; Figures 9c and 9d). The models with longer backstop offsets also exhibit a larger area topographic low along the transfer zone than models with a short backstop offset ($L_B = 20$ km).

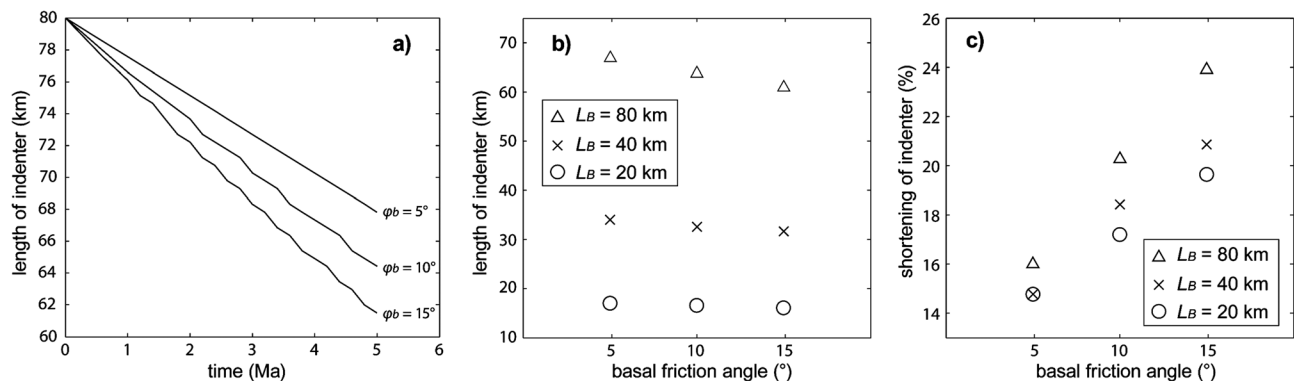


Figure 15. a) Length of the indenter over time for simulations with an initial indenter length of $L_B = 80$ km and basal friction angles of $\varphi_b = 5^\circ$, 10° , and 15° . b) Length of indenters after 5 Ma runtime depending on basal friction angle φ_b and initial indenter length. c) Relative shortening of indenters after 5 Ma runtime depending on basal friction angle φ_b and initial indenter length L_B .

[43] Strain rate patterns illustrate that the wedges deform by plastic failure in narrow shear bands (Figure 10). Independent of the backstop offset, frontal thrusts form symmetric, conjugate shear bands. Active shear bands verging toward the wedge front exhibit higher strain rates than conjugate backthrusts (Figure 10).

[44] Models with identical basal friction angles ($\varphi_b = 5^\circ$) develop differently, depending on the backstop offset. Two major observations merit emphasis: (i) the domain B pushed by the promontory develops a narrower wedge with increasing backstop offset: whereas there are eight thrusts in the model with a backstop offset of $L_B = 20$ km at 5 Ma (Figure 10a), there are seven for an intermediate backstop offset (Figure 10b) and only six in the model with a backstop offset of $L_B = 80$ km (Figure 10c). (ii) Longer backstop offsets lead to wider wedges in domain A (Figure 10).

4.3.2. Medium Basal Friction ($\varphi_b = 10^\circ$)

[45] Models with a basal friction angle of $\varphi_b = 10^\circ$ and different offsets in backstop at 6 Ma differ strongly in their topographic elevation depending on the backstop offset length (Figure 11). The cylindrical model (Figure 11a), matching the critical wedge theory (Figure 7), serves as a reference for the wedges influenced by transfer zones. The main difference between the models with different backstop offsets is the maximal elevation in domain B. For $L_B = 20$ km, the wedge domain B has a higher rear topography than domain A (Figure 11b). Furthermore, this model does not exhibit the topographic low described in previous experiments. In the model with a backstop offset $L_B = 40$ km, maximal elevation is similar in both wedge domains (Figure 11c). A topographic low also appears in domain A, next to the promontory, disconnecting the thrusts in domain B from those in domain A. For the backstop offset $L_B = 80$ km, the maximal elevation is lower in domain B than in domain A (Figure 11d). The thrusts in domain B are strongly curved around the promontory corner, and topographic elevation decreases and fades out toward domain A.

[46] Structurally, wedges with a basal friction angle of $\varphi_b = 10^\circ$ differ from models featuring a décollement friction of $\varphi_b = 5^\circ$. Thrusts in domain B exhibit larger offsets and are clearly verging toward the wedge front for a basal friction angle of $\varphi_b = 10^\circ$ (Figure 12). Like in the low basal friction models, wedges in domain A are increased in profile length with increasing backstop offset. Accordingly, single thrusts

in the model with a backstop offset of $L_B = 20$ km (Figure 12a) exhibit larger offsets than thrusts in the model with a backstop offset of $L_B = 80$ km (Figure 12c).

4.3.3. High Basal Friction ($\varphi_b = 15^\circ$)

[47] In the models with a backstop offset overlying a basal décollement with a friction angle of $\varphi_b = 10^\circ$, the maximal elevation in domain B strongly depends on the offset (Figure 11). In contrast, models with $\varphi_b = 15^\circ$ after a run time of 6 Ma exhibit different maximal elevations in domain A depending on the backstop offset (Figure 13). For $L_B = 20$ km, the maximal rear elevations of both domains are similar at ~ 8 km (Figure 13b). The frontal thrust and major thrust sheets are connected throughout the whole width (y -direction) of the model. With longer backstop offsets, the maximal elevation of the wedge is developed in domain A (Figure 13c). In contrast to models with lower friction angles ($\varphi_b = 5^\circ, 10^\circ$) and a backstop offset of $L_B = 40$ km, the topographic low is smaller. In the model with a backstop offset of $L_B = 80$ km, the maximal elevation in domain A is up to 2 km higher than the maximal elevation in domain B (Figure 13d). Thrust sheets are curved around the promontory corner, and their surface elevation decreases and fades out toward domain A.

[48] Plotted profiles through material phases show that wedges in domain B are wider (x -direction) for a shorter backstop offset (Figure 14a) and get narrower with less thrust sheets for an increasing backstop offset (Figures 14b and 4c). All models mainly exhibit thrusts verging toward the wedge front. For an offset $L_B = 80$ km, the wedges in domain A exhibit shear bands with little finite strain, i.e., a limited offset (Figure 14c). Strain rate patterns in these models show that frontal thrusts are not associated with conjugate faults as in low basal friction models (Figure 10). In addition, forward verging thrusts are flattened and backthrusts are steeper than in previously described models (Figure 14).

4.4. Indenter Deformation

[49] The indenter is compressed along the shortening direction in all experiments. The length of the indenters is decreasing linearly with time, where compression is larger for stronger basal décollements (Figure 15a). Pure shear within the indenter body results in $\sim 10\%$ thickening of close to the rear for all models and is negligible at its front. Most of the subsequent shortening is absorbed in an elongated buckle fold at the rear of the indenter, with a trend

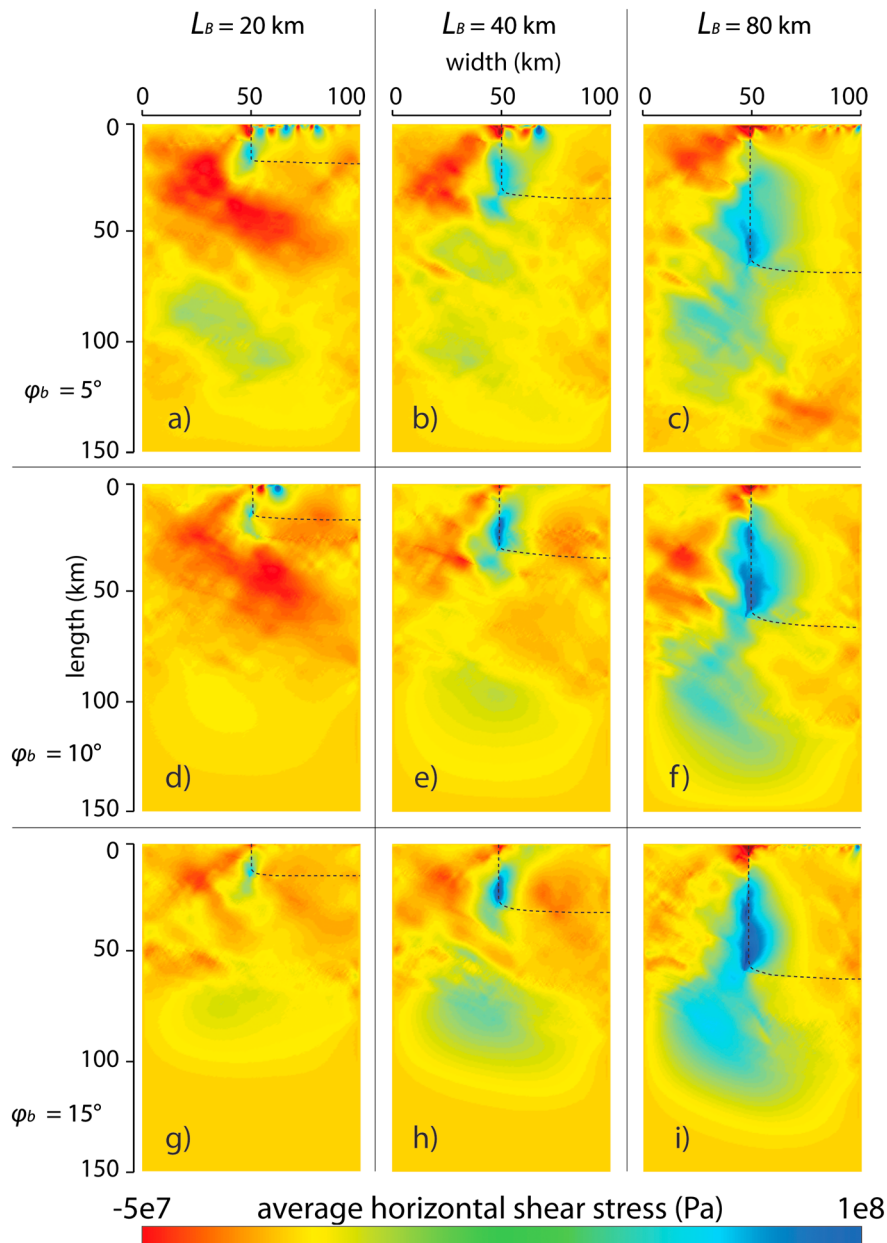


Figure 16. Vertically averaged horizontal shear stresses after 5 Ma run time. Columns for same backstop offset, rows for same basal friction. Positive shear stress values report stress rotation with clockwise rotation in map view. Dashed lines: position of the rigid indenter.

parallel to the model boundary (Figures 8, 9, 11, and 13). The wavelength of the indenter fold depends on its thickness (Figures 10, 12, and 14). The absolute amount of indenter shortening increases with increasing basal friction, as mentioned above. This effect is enhanced for longer backstop offsets (Figure 15b). This is illustrated by the relative shortening of the indenter to its initial length L_B (Figure 15c).

[50] Even though shortening takes place within the indenter, it does not falsify the results in terms of surface slope. The minor deformation of the indenter

lowers the actual shortening velocity within the wedge in front of the indenter. However, because the analytical wedge theory is time independent, and therefore independent of shortening velocity, the expected tapers are equal.

5. Discussion

[51] All modeled wedges grow in-sequence by developing frontal thrust ramps and accreting new material at their front (Figure 6). Structural and

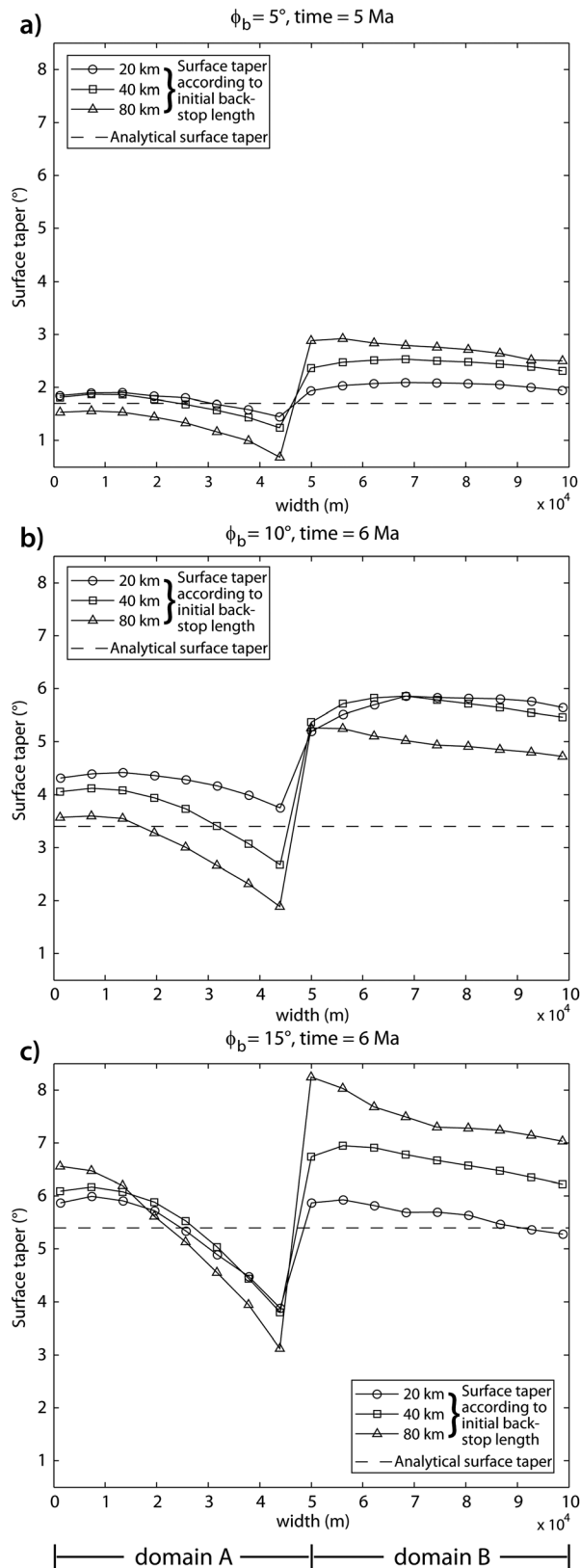


Figure 17. Numerically derived surface tapers over width (y -direction) for simulations with different initial backstop offsets. Circles: $L_B = 20$ km. Squares: $L_B = 40$ km. Triangles: $L_B = 80$ km. Dashed lines: analytically derived minimum critical taper. a) Basal friction angle $\varphi_b = 5^\circ$ at 5 Ma runtime. b) Basal friction angle $\varphi_b = 10^\circ$ at 6 Ma runtime. c) Basal friction angle $\varphi_b = 15^\circ$ at 6 Ma runtime.

morphological variations in simulations without the backstop promontory are related to differences in basal friction. Results confirm numerically, after conclusions from analogue and 2D numerical models, that the rheological strength of the basal décollement is one of the most important factors for the structural and topographic evolution of a thin-skinned compressional thrust wedge. Low basal friction allows very wide (from rear to toe), low tapered fold-and-thrust belts (Figure 4a). The inclination of developing shear bands within the wedge also depends on the basal resistance to shear (Figure 5), as it has been shown in analogue [Davis *et al.*, 1983] and 2D numerical models [Ruh *et al.*, 2012]. In a wedge with low basal friction, the main stress direction remains close to horizontal (Figure 5). In such a stress regime, frontal accretion tends to develop conjugate, symmetric shear bands. The principal, compressional stress directions are increasingly inclined with increased basal friction so that forward verging thrust ramps tend to dip more shallowly and back thrusts more steeply (Figure 5). Therefore, frontal accretion in wedges with high basal friction is defined mainly by frontward verging thrusts and less by back thrusts because compressional shortening due to a low angle thrust is energetically more efficient (less gravitational counterforce and less finite strain in the shear zone for the same amount of shortening).

[52] Tapers obtained in these new simulations match well the analytical solution of the critical wedge theory (Figure 7). Surface slopes for the models with basal friction of $\varphi_b = 5^\circ$ and 10° decrease to the minimum taper at around 3 Ma. Out-of-sequence thrusts close to the rear of the models balance tapers that reach the minimum critical taper (Figure 4) and surface slope increases. The model with $\varphi_b = 15^\circ$ does not reach the critical minimum after 7 Ma (Figure 7) but is in the stable field, accreting new material at its front. This indicates that the critical wedge theory is applicable to 3D numerical models with a linear backstop.

[53] Simulations with offset backstops demonstrate the influence of predefined transfer zones on the evolution of critical wedges. In models with identical frictional strength but differing length of the promontory, shapes of wedges vary laterally in terms of topography and wedge length. For low basal friction (Figure 9), the wedge tapers in domain A decrease in maximal elevation with increasing backstop offsets. For intermediate basal friction (Figure 11), elevations in domain A remain similar for different backstop offsets, whereas the average width (from rear to toe) of the wedges in front of the promontory (domain B) decrease with increasing backstop offset. Models with a strong base (Figure 13) show higher maximal elevation in domain A for longer backstop offsets.

[54] The fact that lateral structural variations exist for different basal strengths demonstrates that the structural evolution along transfer zones is influenced by both the length of the backstop offset and the frictional strength of the basal décollement. Competition between lateral (horizontal shear strain; xy -plane) and basal (shear strain in the xz -plane) drag controls the wedge tapers in both parts of the wedge. The wedges in domain B exhibit a slower growth in x -direction than those in the adjacent domain A (Figure 8). This produces narrower wedges and therefore steeper taper surfaces in front of the promontory. The effects that the offset length of the backstop and the basal friction have together can be roughly quantified by the vertically averaged horizontal shear stresses $\bar{\tau}_{xy}$ at 5 Ma run time. In all simulations, positive shear stresses (clockwise-rotated in the presented map view) are largest along the wall of the indenter at $y = 50$ km (Figure 16). The area of large positive shear stresses ($\bar{\tau}_{xy} > 5 \cdot 10^7$ Pa) increases with indenter length; maximum shear stress magnitudes increase as well (e.g., Figures 16g–16i). These magnitudes also increase with increasing basal friction (e.g., Figures 16c, 16f, and 16i). Overall, the length of the backstop offset has a larger influence on horizontal shear stresses than basal strength and has therefore a more pregnant influence on the structural evolution along transfer zones.

[55] The influence of the backstop offset on the slope of the wedge surface is illustrated by plotting taper angles α at different y -coordinates for the different basal strengths (Figure 17). In general, surface slopes decrease from $y = 0$ km toward the transfer zone at $y = 50$ km. Wedges in domain B ($y = 50 - 100$ km) are steeper than the predicted analytical solution. Furthermore, surface slopes in

front of the promontory are increased with increasing backstop offset as well as with increasing basal friction (Figure 17). This matches the observations made from horizontal shear stresses. The stronger the basal décollement and the longer the backstop offset, the larger are horizontal shear stresses (Figure 16). Horizontal shear stresses along the indenter indicate lateral drag (horizontal shear strain; xy -plane). This lateral drag along the indenter supports wider and flatter wedges than the analytical solution in domain A and narrower and steeper wedges in domain B. This consists with taper measurements of simulations with indenters (Figure 17).

5.1. Comparison to Previous Modeling Studies

[56] Simulations of 3D cylindrical setups (Figure 4) can be compared to previous 2D numerical models. Several numerical approaches have simulated thin-skinned compressional thrust wedges with brittle/plastic rheology over the last decade. In terms of sequential formation of thrust sheets, orientation of high strain rate shear bands and the authentication of the critical wedge theory, profiles of our simulations compare well to 2D numerical models [Buiter, 2012; Buiter *et al.*, 2006; Ruh *et al.*, 2012; Selzer *et al.*, 2007; Simpson, 2011].

[57] Transfer zones in compressional thrust wedges have mainly been investigated by analogue models [Calassou *et al.*, 1993; Experiment 2] with the backstop offset constructed parallel to the bulk shortening direction. In these analogue models, both sides of the transfer zone developed similar tapers. This indicates that the basal strength had a larger influence than horizontal drag along the edge of the indenter. This is verified by the rather high basal friction angle (18°) compared to the internal friction angle (30°) they applied in this experiment.

[58] Our results, like analogue models [Macedo and Marshak, 1999; Figure 12d], have shown that the initial offset in the deformation front tends to be absorbed into a linear frontal thrust orthogonal to the bulk shortening direction.

[59] Analogue models of Reiter *et al.* [2011] applied lateral variations in backstop velocity instead of a rigid backstop reaching into the model domain. They employed very high basal friction angles ($22.3^\circ < \varphi_b < 29.2^\circ$) for an initial internal friction angle of $\varphi = 35.4^\circ$, comparable to our model setup with a basal friction angle of $\varphi_b = 15^\circ$ (Figure 13).

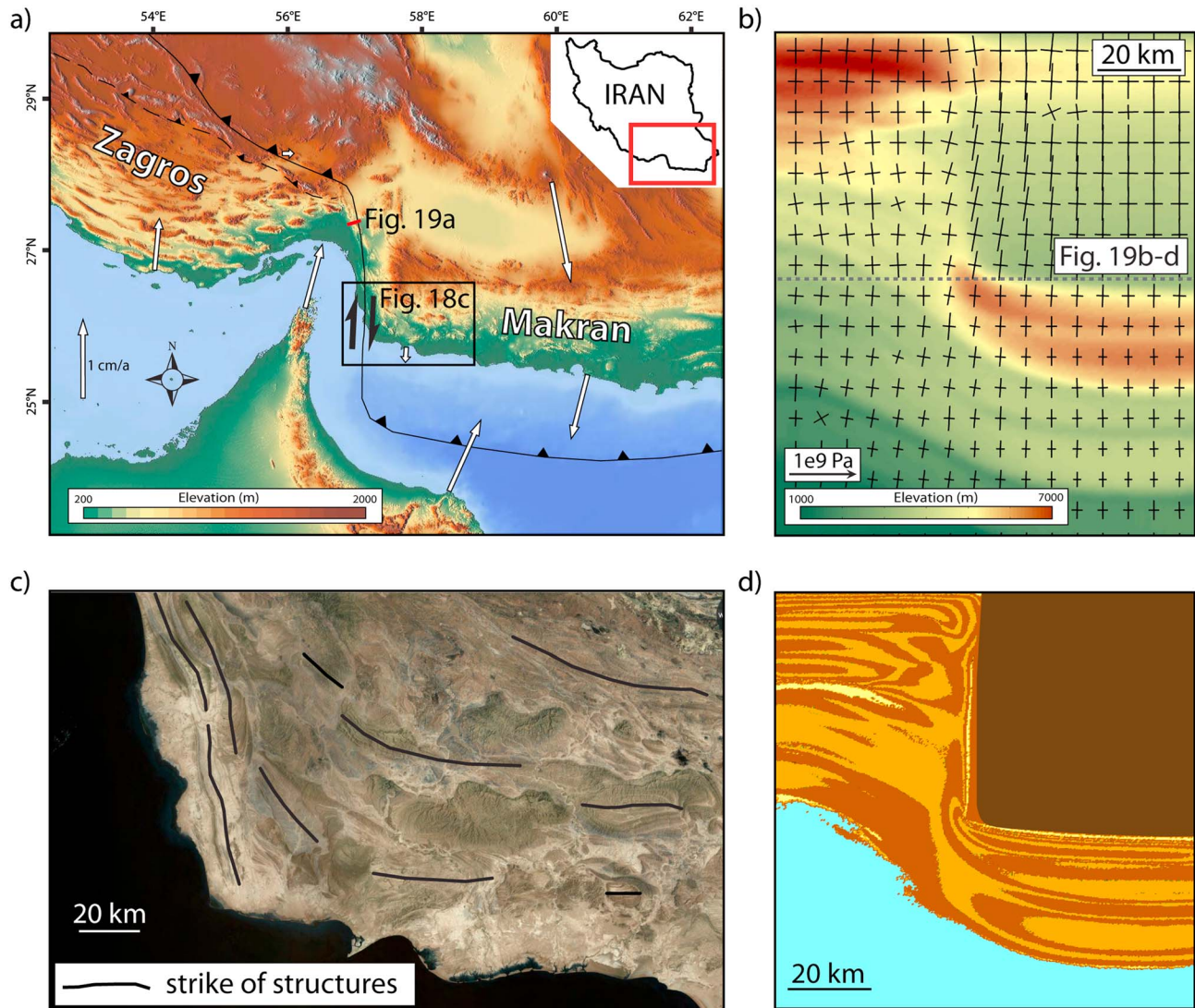


Figure 18. Comparison of numerical results with the Zagros-Makran transition zone. a) Elevation map of SE Iran, indicating the most important plate boundaries with the right lateral Minab-Zendan fault system in the center. White arrows: horizontal GPS velocities for a rigid Central Iranian Block [Vernant *et al.*, 2004]. Black box: location of subfigure (c). b) Elevation plot of numerical simulation with a basal friction of $\varphi_b = 10^\circ$ and an initial backstop length of $L_B = 80$ km after 6 Ma runtime. Black arrows: vertically averaged stresses. Dashed line: location of the slices in Figure 19b–19d. c) Satellite picture indicating major structural strike directions. d) Horizontal slice at an elevation of 6300 m of the numerical simulation with a basal friction of $\varphi_b = 10^\circ$ and an initial backstop length of $L_B = 80$ km after 6 Ma run time. Plotted Lagrangian markers indicate strong bending of structure axes at the promontory corner.

The main difference in topography evolution is that, in their work, the wedge in front of the faster backstop segment is larger than that in front of the slow backstop [Reiter *et al.*, 2011; Figure 8]. In our simulations, the wedge parts in domain A exhibit higher elevations and are longer from rear to toe in contrast to wedges in domain B. These observations vary with different backstop offsets (Figure 13). The development of strike-slip shear zones in analogue simulations, but not in the 3D numerical simulations, explains this discrepancy. High strain rate shear

zones along the transfer zone would release shear stresses. We contend that vertically dipping strike-slip faults would spontaneously occur in numerical simulations if we had implemented strain or strain-rate weakening.

[60] A 3D numerical model with a similar geometrical setup was presented by Braun and Yamato [2010]. A major difference, though, is that they induced a vertical strike-slip zone along the transfer zone by their formulation of the velocity boundary

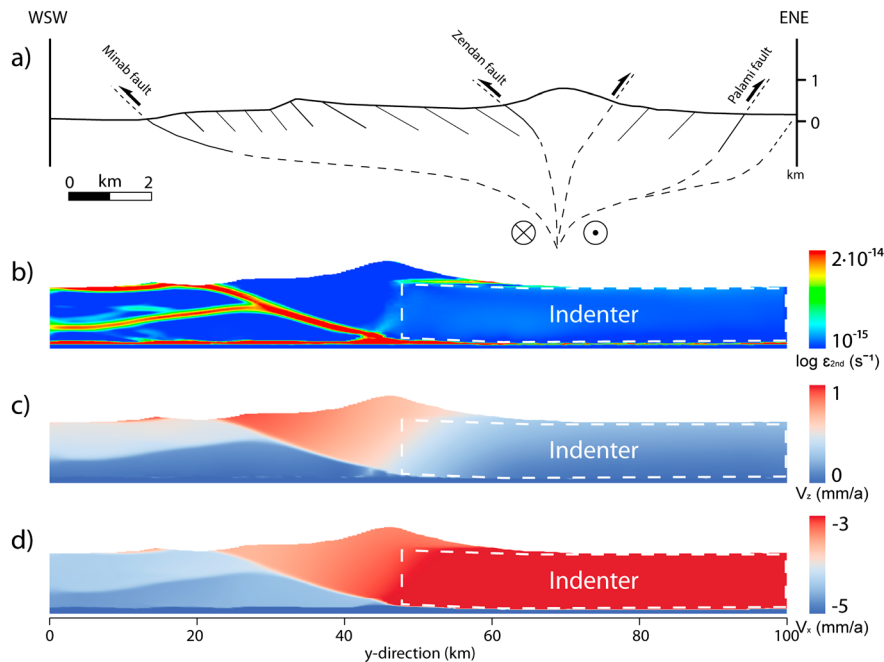


Figure 19. a) Profile cutting the Minab-Zendan right lateral fault system [after *Regard et al.*, 2004; *Smith et al.*, 2005]. Location is shown in Figure 18a. Subfigures b) to d) slices of numerical simulations with a basal friction of $\varphi_b = 10^\circ$ and an initial backstop length of $L_B = 80$ km after 6 Ma runtime. From $y = 50 - 100$ km slices cut the rigid promontory. Location of profiles b) to d) shown in Figure 18b). b) Second invariant of the strain rate tensor. c) Vertical velocity, upward movement. d) Horizontal velocity in x -direction, motion toward the backstop negative.

conditions. In their paper, they mainly investigated the orogenic (triangular pop-up structure) response to the surface evolution. They document a curvature of the evolving thrust sheet and of the frontal fault as reported in our results.

5.2. Comparison to Natural Examples

[61] Results indicate that the structural and topographic evolutions of thin-skinned wedges are strongly influenced by both the backstop indentation and the strength of the basal décollement. We compare our model results to the Zagros-Makran transition zone, which separates the Makran accretionary wedge in the east from the Zagros foreland fold-and-thrust belt in the west [*Peyret et al.*, 2009; *Regard et al.*, 2004; *Regard et al.*, 2005; *Smith et al.*, 2005]. The ~ 300 km long dextral Minab-Zendan fault system strikes close to N-S, nearly parallel to the convergence direction between Arabia and Eurasia [*Vernant et al.*, 2004] (Figure 18a). The Makran represents a submarine accretionary wedge, evolved by scraping crustal material off the subducting Arabian oceanic plate [*McCall*, 2002; *Platt*, 1990]. On the other hand, the Zagros Folded belt results from the continental collision between Arabia and Eurasia [*Agard et al.*, 2011; *Stocklin*,

1968]. In the Makran, the major décollement layer is formed by overpressured shale [*Platt*, 1990]. Opposed to that, the Zagros Folded belt is detached from the basement along an initially 1 km, locally up to 2 km thick salt horizon, the Hormuz salt [*Kent*, 1958; *Talbot*, 1998]. Nevertheless, we here want to show that topographic and structural features along the Zagros-Makran transition zone can be independent of the appearing transitions in décollement and sequence rheology.

[62] At the southeastern end of the Zagros, the fold belt is narrow to almost not existent, fading out toward the Zagros-Makran transition zone (Figure 18a). This narrowing of the fold belt coincides with a topographic low to the west of the Minab-Zendan fault. In the numerical simulation ($\varphi_b = 10^\circ$, $L_B = 80$ km at 6 Ma), we pointed out the topographic low that appears in the wedges along the promontory side. The wedge taper in domain A is not cylindrical, and high elevations show a triangular zone, fading out toward the transfer zone (Figure 18b). Furthermore, numerically derived horizontal main stress directions (black arrow in Figure 18b) at 1 km depth compare well with reported stress directions calculated from inversion of striation measurements [*Regard et al.*, 2004].

[63] Folds in western Makran, close to the Minab-Zendan fault zone, are strongly influenced by the dextral Minab-Zendan fault system (Figure 18c). They trend W-E, orthogonal to the bulk shortening direction for most of the length of Makran. In the west, folds turn to trend parallel to the N-S Minab-Zendan strike slip fault system. A similar change in structural trend occurs in our simulations. A horizontal slice (xy -plane), cutting at 8600 m (z -direction; where zero is the bottom of the Eulerian grid), shows material phases (brown and orange colors represent initially layered sequence as in Figure 6; Figure 18d). Folds are curved around the promontory corner and strike parallel to the bulk shortening direction along the transfer zone.

[64] A roughly W-E geological profile through the northern part of the dextral Minab-Zendan fault system displays several reverse faults defining a positive flower structure (Figure 18a). Vertical slices through the numerical simulation presented in Figure 18b ($\varphi_b = 10^\circ$, $L_B = 80$ km at 6 Ma) are cutting the Eulerian grid orthogonal to both the bulk shortening direction and the transfer zone. The second invariant of the strain rate tensor (Figure 19b) exhibits a flat shear zone that roots into the basal décollement right below the predefined transfer zone ($y = 50$ km). A topographic high appears atop the fault root. The topography in the numerical model and the flat thrust geometrically resemble the geological profile. Vertical velocities (Figure 19c) indicate that the hanging wall is uplifted. Plotted horizontal velocities (Figure 19d) parallel to the bulk shortening (x -direction) reveal a right lateral movement along this fault. According to the plotted velocities, the low-angle shear zone acts as an oblique thrust. This is also reported along the Minab fault [Regard *et al.*, 2004] (Figure 19a).

[65] The models presented here simulate general features of the Zagros-Makran transition zone, especially in terms of surface topography and thrust orientation. We acknowledge that differences in décollement type (salt in Zagros, shale in Makran) may also influence the overall mechanics along this transfer zone. However, this study shows that first-order features such as surface topography and thrust orientation may be more independent of décollement type and/or variations in rock sequence than advocated by some authors.

6. Conclusion

[66] A high-resolution 3D finite difference numerical model with a visco-plastic rheology was created and

employed to investigate how the frictional strength of a décollement affects the development of thin-skinned compressional fold-and-thrust belts along transfer zones. Compression of sedimentary rocks above a frictional décollement leads to forward, in-sequence thrusting, forming ramps with dip angles depending on the within-wedge stress directions, which can be analytically derived. Perfectly cylindrical simulations correlate well with the critical wedge theory.

[67] An offset backstop was simulated with a rigid, rectangular promontory added to the cylindrical setup. This promontory strongly influences the evolution of the thin-skinned brittle wedge. Wedge tapers in front of the promontory tend to exceed the analytically derived tapers. Surface slopes in domain A, where no promontory exists, are lower than the analytical prediction. In this domain, single thrust zones exhibit less offset, which leads to more scattered structural patterns. Wedges in front of the promontory structurally differ from the wedges that form where no promontory is present. The wedges pushed by the promontory usually form steeper surface slopes and build thrust sheets with large fault offsets. The impact of the transition zone on the surface tapers of both simulation domains, the one pushed by the promontory and the other by the grid boundary, increases with increasing basal décollement strength.

[68] These new 3D numerical simulations explain the occurrence of folds parallel to the shortening direction as observed in the Zagros-Makran transfer/transform zone. The low angle faulting with a lateral component similar to the Minab fault was reproduced. Importantly, our simple geometrical setup has shown how topographic lows like that observed north of the Strait of Hormuz, in the Zagros, can be produced in compressional settings. Such lows (intramontane basins) are indicative for transfer zones in particular.

Acknowledgement

[69] This work was supported by Swiss National Fonds grant 2-77644-09. Taras Gerya was supported by the Crystal2Plate, the SNF ProDoc, and the 4-D-Adamello and TopoEurope program. Many thanks go to Susanne Buitter and Markus Albertz for their constructive review.

References

Agard, P., J. Omrani, L. Jolivet, H. Whitechurch, B. Vrielynck, W. Spakman, P. Monie, B. Meyer, and R. Wortel (2011),

- Zagros orogeny: a subduction-dominated process, *Geol. Mag.*, 148(5-6), 692–725.
- Allken, V., R. S. Huismans, and C. Thieulot (2011), Three-dimensional numerical modeling of upper crustal extensional systems, *J. Geophys. Res.-Sol. Ea.*, 116 B10409, doi:10.1029/2011JB008319.
- Arthur, J. R. F., T. Dunstan, Q. A. J. Al-Ani, and A. Assadi (1977), Plastic deformation and failure of granular media, *Géotechnique*, 27, 53–74.
- Beaumont, C., P. Fullsack, and J. Hamilton (1992), Erosional Control of Active Compressional Orogens, *Thrust Tectonics*, 1–18.
- Braun, J., and P. Yamato (2010), Structural evolution of a three-dimensional, finite-width crustal wedge, *Tectonophysics*, 484(1-4), 181–192.
- Braun, J., C. Thieulot, P. Fullsack, M. DeKool, C. Beaumont, and R. Huismans (2008), DOUAR: A new three-dimensional creeping flow numerical model for the solution of geological problems, *Phys. Earth Planet In.*, 171(1-4), 76–91.
- Buiter, S. J. H. (2012), A review of brittle compressional wedge models, *Tectonophysics*, 530, 1–17.
- Buiter, S. J. H., A. Y. Babeyko, S. Ellis, T. V. Gerya, B. J. P. Kaus, A. Kellner, G. Schreurs, and Y. Yamada (2006), The numerical sandbox: Comparison of model results for a shortening and an extension experiment, *Geol. Soc. Spec. Publ.*, 253, 29–64.
- Burbidge, D. R., and J. Braun (2002), Numerical models of the evolution of accretionary wedges and thrust-and-fold belts using the distinct element method (vol 148, pg 542, 2002), *Geophys. J. Int.*, 151(3), 957–957.
- Calassou, S., C. Larroque, and J. Malavieille (1993), Transfer Zones of Deformation in Thrust Wedges - an Experimental Study, *Tectonophysics*, 221(3-4), 325–344.
- Chapple, W. M. (1978), Mechanics of thin-skinned fold-and-thrust belts, *Geol. Soc. Am. Bull.*, 89(8), 1189–1198.
- Coulomb, C. A. (1773), L'application des règles, de maximis et minimis à quelque problèmes de statique, relatifs à l'architecture, *Mémoires de Mathématique et de Physique, Academie Royale des Sciences*, 7, 343–382.
- Cramer, F., H. Schmeling, G. J. Golabek, T. Duretz, R. Orendt, S. J. H. Buiter, D. A. May, B. J. P. Kaus, T. V. Gerya, and P. J. Tackley (2012), A comparison of numerical surface topography calculations in geodynamic modelling: an evaluation of the 'sticky air' method, *Geophys. J. Int.*, 189(1), 38–54.
- Dahlen, F. A. (1984), Noncohesive Critical Coulomb Wedges - an Exact Solution, *J. Geophys. Res.*, 89(Nb12), 125–133.
- Dahlen, F. A. (1990), Critical taper model of fold-and-thrust belts and accretionary wedges, *Annu. Rev. Earth. Pl. Sc.*, 18, 55–99.
- Dahlen, F. A., J. Suppe, and D. Davis (1984), Mechanics of fold-and-thrust belts and accretionary wedges - cohesive coulomb theory, *J. Geophys. Res.*, 89(Nb12), 87–101.
- Davis, D., and T. Engelder (1985), The role of salt in fold-and-thrust belts, *Tectonophysics*, 119(1-4), 67–88.
- Davis, D., J. Suppe, and F. A. Dahlen (1983), Mechanics of Fold-and-Thrust Belts and Accretionary Wedges, *J. Geophys. Res.*, 88(Nb2), 1153–1172.
- Fillon, C., R. S. Huismans, and P. van der Beek (2013), Syntectonic sedimentation effects on the growth of fold-and-thrust belts, *Geology*, 41, pp. 83–86, doi: 10.1130/G33531.1.
- Gerya, T. (2010a), Dynamical Instability Produces Transform Faults at Mid-Ocean Ridges, *Science*, 329(5995), 1047–1050.
- Gerya, T. (2010b), *Introduction to Numerical Geodynamic Modelling*, 345 pp., Cambridge University Press, Cambridge, UK.
- Gerya, T. V., and D. A. Yuen (2003), Rayleigh-Taylor instabilities from hydration and melting propel 'cold plumes' at subduction zones, *Earth Planet. Sci. Lett.*, 212(1-2), 47–62.
- Gerya, T., and D. A. Yuen (2007), Robust characteristics method for modelling multiphase visco-elasto-plastic thermo-mechanical problems, *Phys Earth Planet In.*, 163(1-4), 83–105.
- Graveleau, F., J. Malavieille, and S. Dominguez (2012), Experimental modelling of orogenic wedges: A review, *Tectonophysics*, 1-66.
- Hilley, G. E., and M. R. Strecker (2004), Steady state erosion of critical Coulomb wedges with applications to Taiwan and the Himalaya, *J. Geophys. Res.-Sol. Ea.*, 109(B1).
- Huiqi, L., K. R. McClay, and D. Powell (1992), Physical models of thrust wedges., in *Thrust Tectonics*, edited by K. R. McClay, pp. 71–81, Chapman and Hall, New York.
- Kaus, B. J. P. (2010), Factors that control the angle of shear bands in geodynamic numerical models of brittle deformation, *Tectonophysics*, 484(1-4), 36–47.
- Kent, P. E. (1958), Recent studies of south Persian salt plugs, *Am. Assoc. Pet. Geol. Bull.*, 422, 2951–2972.
- Konstantinovskaya, E., and J. Malavieille (2011), Thrust wedges with decollement levels and syntectonic erosion: A view from analog models, *Tectonophysics*, 502(3-4), 336–350.
- Koons, P. O. (1990), 2-Sided Orogen - Collision and Erosion from the Sandbox to the Southern Alps, New-Zealand, *Geology*, 18(8), 679–682.
- Kopf, A., and K. M. Brown (2003), Friction experiments on saturated sediments and their implications for the stress state of the Nankai and Barbados subduction thrusts, *Mar. Geol.*, 202(3-4), 193–210.
- Macedo, J., and S. Marshak (1999), Controls on the geometry of fold-thrust belt salients, *Geol. Soc. Am. Bull.*, 111(12), 1808–1822.
- McCall, G. J. H. (2002), A summary of the geology of the Iranian Makran, *Tectonic Clim. Evol. Arabian Sea Reg.*, 195, 147–204, 525.
- Morley, C. K. (1988), Out-of-sequence thrusts, *Tectonics*, 7(3), 539–561.
- Mulugeta, G. (1988), Modeling the geometry of coulomb thrust wedges, *J. Struct. Geol.*, 10(8), 847–859.
- Nilfroushan, F., H. A. Koyi, J. O. H. Swantesson, and C. J. Talbot (2008), Effect of basal friction on surface and volumetric strain in models of convergent settings measured by laser scanner, *J. Struct. Geol.*, 30(3), 366–379.
- Nilfroushan, F., R. Pysklywec, and A. Cruden (2012), Sensitivity analysis of numerical scaled models of fold-and-thrust belts to granular material cohesion variation and comparison with analog experiments, *Tectonophysics*, 526, 196–206.
- Peyret, M., et al. (2009), Present-day strain distribution across the Minab-Zendan-Palami fault system from dense GPS transects, *Geophys. J. Int.*, 179(2), 751–762.
- Platt, J. P. (1990), Thrust mechanics in highly overpressured accretionary wedges, *J. Geophys. Res.-Solid*, 95(B6), 9025–9034.
- Popov, A. A., and S. V. Sobolev (2008), SLIM3D: A tool for three-dimensional thermo mechanical modeling of lithospheric deformation with elasto-visco-plastic rheology, *Phys. Earth Planet In.*, 171(1-4), 55–75.
- Regard, V., O. Bellier, J. C. Thomas, M. R. Abbassi, J. Mercier, E. Shabanian, K. Feghhi, and S. Soleymani (2004), Accommodation of Arabia-Eurasia convergence in the Zagros-Makran transfer zone, SE Iran: A transition between collision and subduction through a young deforming system, *Tectonics*, 23(4).
- Regard, V., et al. (2005), Cumulative right-lateral fault slip rate across the Zagros-Makran transfer zone: role of

- the Minab-Zendan fault system in accommodating Arabia-Eurasia convergence in southeast Iran, *Geophys. J. Int.*, *162*(1), 177–203.
- Reiter, K., N. Kukowski, and L. Ratschbacher (2011), The interaction of two indenters in analogue experiments and implications for curved fold-and-thrust belts, *Earth Planet. Sci. Lett.*, *302*(1–2), 132–146.
- Roscoe, K. H. (1970), The influence of strains in soil mechanics, *Géotechnique*, *20*, 129–170.
- Ruh, J. B., B. J. P. Kaus, and J. P. Burg (2012), Numerical investigation of deformation mechanics in fold-and-thrust belts: Influence of rheology of single and multiple décollements, *Tectonics*, *31*.
- Saffer, D. M., K. M. Frye, C. Marone, and K. Mair (2001), Laboratory results indicating complex and potentially unstable frictional behavior of smectite clay, *Geophys. Res. Lett.*, *28*(12), 2297–2300.
- Schenk, O., and K. Gartner (2004), Solving unsymmetric sparse systems of linear equations with PARDISO, *Future Gener. Comp. Sy.*, *20*(3), 475–487.
- Schenk, O., and K. Gartner (2006), On fast factorization pivoting methods for sparse symmetric indefinite systems, *Electron. T. Numer. Ana.*, *23*, 158–179.
- Schmeling, H., et al. (2008), A benchmark comparison of spontaneous subduction models-Towards a free surface, *Phys. Earth Planet. In.*, *171*(1–4), 198–223.
- Selzer, C., S. J. H. Buiter, and O. A. Pfiffner (2007), Sensitivity of shear zones in orogenic wedges to surface processes and strain softening, *Tectonophysics*, *437*(1–4), 51–70.
- Simpson, G. D. H. (2009), Mechanical modelling of folding versus faulting in brittle-ductile wedges, *J. Struct. Geol.*, *31*(4), 369–381.
- Simpson, G. D. H. (2011), Mechanics of non-critical fold-thrust belts based on finite element models, *Tectonophysics*, *499*(1–4), 142–155.
- Smith, B., C. Aubourg, J. C. Guezou, H. Nazari, M. Molinaro, X. Braud, and N. Guya (2005), Kinematics of a sigmoidal fold and vertical axis rotation in the east of the Zagros-Makran syntaxis (southern Iran): Paleomagnetic, magnetic fabric and microtectonic approaches, *Tectonophysics*, *411*(1–4), 89–109.
- Stocklin, J. (1968), Structural history and tectonics of Iran: a review, *Am. Assoc. Pet. Geol. Bull.*, *52*, 1223–1258.
- Stockmal, G. S. (1983), Modeling of large-scale accretionary wedge deformation, *J. Geophys. Res.*, *88*(Nb10), 8271–8287.
- Stockmal, G. S., C. Beaumont, M. Nguyen, and B. Lee (2007), Mechanics of thin-skinned fold-and-thrust belts: Insights from numerical models, *Geol. Soc. Am. Spec. Pap.*, *433*, 63–98.
- Storti, F., and K. McClay (1995), Influence of syntectonic sedimentation on thrust wedges in analog models, *Geology*, *23*(11), 999–1002.
- Takahashi, M., K. Mizoguchi, K. Kitamura, and K. Masuda (2007), Effects of clay content on the frictional strength and fluid transport property of faults, *J. Geophys. Res.-Sol. Ea.*, *112*(B8).
- Talbot, C. J. (1998), Extrusions of Hormuz salt in Iran, *Lyell: The Past Is the Key to the Present*, *143*, 315–334.
- Vernant, P., et al. (2004), Present-day crustal deformation and plate kinematics in the Middle East constrained by GPS measurements in Iran and northern Oman, *Geophys. J. Int.*, *157*(1), 381–398.
- Wang, C. Y., N. H. Mao, and F. T. Wu (1980), Mechanical-properties of clays at high-pressure, *J. Geophys. Res.*, *85* (Nb3), 1462–1468.
- Westbrook, G. K., and M. J. Smith (1983), Long décollements and mud volcanos - Evidence from the Barbados Ridge Complex for the role of high pore-fluid pressure in the development of an accretionary complex, *Geology*, *11*(5), 279–283.
- Zaleski, S., and P. Julien (1992), Numerical-simulation of Rayleigh-Taylor instability for single and multiple salt diapirs, *Tectonophysics*, *206*(1–2), 55–69.
- Zhu, G. Z., T. V. Gerya, D. A. Yuen, S. Honda, T. Yoshida, and J. A. D. Connolly (2009), Three-dimensional dynamics of hydrous thermal-chemical plumes in oceanic subduction zones, *Geochem. Geophys. Geosy.*, *10*, 1–20, doi:10.1029/2009GC002635.